Initiations of Mesoscale Convective Systems in the Middle Reaches of the Yangtze River Basin Based on FY-4A Satellite Data: Statistical Characteristics and Environmental Conditions

Yanan Fu[1, 2], Jianhua Sun[1, 2, 3], Shenming Fu[4], Yuanchun Zhang[1], Zheng Ma[1]

[1] Key Laboratory of Cloud-Precipitation Physics and Severe Storms, Institute of Atmospheric Physics, Chinese Academy of Sciences, Beijing, China

[2] University of Chinese Academy of Sciences, Beijing, China

[3] Collaborative Innovation Center on Forecast and Evaluation of Meteorological Disasters, Nanjing University of Information Science and Technology, Nanjing, Jiangsu Province, China

[4] International Center for Climate and Environment Sciences, Institute of Atmospheric Physics, Chinese Academy of Sciences, Beijing, China

Corresponding author: Dr. Jian-Hua Sun (sjh@mail.iap.ac.cn)

Key Points

- The initiations of mesoscale convective systems are backward tracked through a hybrid method of areal overlapping and optical flow
- Quasistationary and outward-moving mesoscale convective systems show notably different characteristics and initiation mechanisms
- A synoptic circulation pattern associated with the Mei-yu front is most favorable for the initiation of mesoscale convective systems

Abstract

Based on the brightness temperature observed by the Fengyun-4A satellite, around eight hundred mesoscale convective systems (MCSs) are identified in the middle reaches of the Yangtze River Basin during the warm seasons (April–September) of 2018–2021, which are categorized into the quasistationary (QS) type and the outward-moving (OM; i.e., vacating the source region) type. Afterward, the initiations of the MCSs are backward tracked using a hybrid method of areal overlapping and optical flow. Then, the main features of QS and OM MCSs and their respective synoptic circulations and environmental parameters are analyzed. The QS MCSs primarily occur in July and August and are mainly initiated in the afternoon. The OM MCSs mostly occur in June and July with two initiation peaks appeared at noon and late night, respectively. The QS MCSs are mainly initiated in mountainous areas, and they are primarily caused by local thermal effects. In contrast, the OM MCSs are mainly initiated in plain areas under synoptic forcings. Circulations of a total of 285 days (without direct influencings from tropical cyclones) are objectively classified into three patterns by using the k-means algorithm. Pattern-I (128 days) which is closely related to low-level jets, shows the most similar features to those of typical Mei-yu fronts, and it acts as the most favorable circulation type for MCSs' initiations. Pattern-II (66 days) is dominated by northwesterlies, with a relatively stable layer in the low-level troposphere. Pattern-III (91 days) features a dry-adiabatic or even a superadiabatic layer that contributes to lowering the layer stability.

Plain Language Summary

Mesoscale convective systems (MCSs) often cause severe convective weather over the middle reaches of the Yangtze River Basin and pose a great threat to life and property in this region. This study identified and tracked MCSs using satellite data and categorized them into the quasistationary (QS) type and the outward-moving (OM) type based on their movement features. The QS type primarily occurs in July and August and is mainly initiated in the afternoon over mountains, caused by local thermal effects. The OM type mostly occurs in June and July and is mainly initiated at noon and late night over the plains, which is related to large-scale circulation. Large-scale circulation regulates environmental conditions and further affects the initiation of MCSs. Circulations over the middle reaches of the Yangtze River Basin are classified into three

patterns, each of which is dominated by a large-scale weather system. The circulation pattern dominated by the Mei-yu front is the most favorable for MCS initiation. The circulation pattern dominated by the northwesterly is favorable for the initiation of OM MCSs but not for QS MCSs. The circulation pattern dominated by the southerly produces a strong thermal effect and is favorable for the initiation of QS MCSs.

1 Introduction

Severe convective weather phenomena, such as heavy rainfall, hailstorms, wind gusts and tornadoes, are mainly associated with mesoscale convective systems (MCSs) (Houze, 2004; Maddox, 1980; Zheng et al., 2013). The generalized concept of the MCS usually covers a broad spectrum of temporal and spatial scales (Yang et al., 2015), and MCSs exhibit different forms if different techniques of detection and identification are employed. In conventional weather maps, MCSs are generally presented as mesoscale high/low pressures (Zipser, 1977). Based on precipitation observations, MCSs often appear as mesoscale rain clusters or belts (Shen et al., 2020). However, MCSs usually appear as different radar reflectivity morphologies (Gallus et al., 2008; Ma et al., 2021a; Yang & Sun, 2018). On satellite infrared images, MCSs often appear as cold-cloud shields (CCSs) with a certain temporal and spatial scale (Laing & Fritsch, 1997; Machado et al., 1998; Meng et al., 2021; Yang et al., 2015; Zheng et al., 2008).

Using the criteria of brightness temperature and cloud area, Maddox (1980) detected a kind of meso-α scale convective system, which was later known as the mesoscale convective complex (MCC), and since then, the method based on the criteria of brightness temperature and cloud area has been widely used in research on MCCs (Laing & Fritsch, 1997; Miller & Fritsch, 1991; Rodgers et al., 1983; Velasco & Fritsch, 1987). Augustine and Howard (1988) simplified the method of Maddox (1980) and found that applying the criteria of brightness temperature ≤ -52 °C and cloud area $\geq 5\times10^4$ km^2 could better describe the evolution of storms. In recent years, −52 °C has been used as the brightness temperature criterion to identify MCSs (Kukulies et al., 2021; Morake et al., 2021; Yang et al., 2015; Yang et al., 2020; Meng et al., 2021), and different cloud area and duration criteria have been applied to determine the spatial and temporal scales of MCSs.

Williams and Houze (1987) developed an algorithm to track an individual cloud cluster in two successive infrared images by calculating the overlapping rate of the two

cloud areas, and since then, the areal overlapping method has been widely used in MCS tracking. Morel and Senesi (2002) improved the accuracy of MCS tracking by estimating the movement of clouds and developed the ISIS (instrument de suivi dans l'imagerie satellitaire) algorithm. Feng et al. (2018) improved the tracking accuracy by expanding the area of the target cloud and developed the FLEXTRKR (flexible object tracker) algorithm. In addition, the optical flow approach has been widely used since it was introduced into meteorology research, including the nowcasting of precipitation (Bowler et al., 2004; Bechini & Chandrasekar, 2017; Bowler et al., 2004) and the improvement of numerical forecast results (Marzban & Sandgathe, 2010). In recent years, the optical flow approach has been applied in the research of new generation geostationary satellite products. Vandal and Nemani (2020) improved the temporal resolution of 10.8 μm infrared longwave radiation products of the new generation Geostationary Operational Environmental Satellite from 15 min to 1 min using the optical flow approach, and they successfully captured the evolution of a severe convective event. Burton et al. (2022) applied the optical flow approach to satellite-retrieved rainfall rate products for West Africa, and extrapolations showed useful skill at up to 4 h of lead time. In the present study, the areal overlapping method is used to track MCSs, and the optical flow is calculated to help improve accuracy.

Previous studies have mainly focused on the process from the formation to the termination of an MCS. Due to the data resolution and technical method limitations, few studies have focused on the initiation of an MCS. Roberts and Rutledge (2003) suggested that the precursor signal of convection initiation (CI) can be captured on satellites. Subsequently, two algorithms for identifying precursor signals and predicting CI based on satellite observations were developed, namely, the SATCAST (satellite convection analysis and tracking algorithm) algorithm (Mecikalski & Bedka, 2006) and the UWCI (University of Wisconsin Convective Initiation) algorithm (Sieglaff et al., 2011). Both scientific research and operational practice have shown that the initiation of MCSs can be identified through satellite observations.

As mentioned above, MCSs have a wide spectrum of spatial and temporal scales, and the features of MCSs, such as the cloud extent, cloud top temperature and cloud motion, vary worldwide (Feng et al., 2019; Kolios & Feidas, 2010; Morel & Senesi, 2002; Punkka & Bister, 2015; Rehbein et al., 2018). The activities of MCSs in China have regional characteristics: the highest frequency of MCSs over the Tibetan Plateau

occurs in July (Zhang et al., 2021; Jiang & Fan, 2002; Mai et al., 2020) and formed mainly in the afternoon (Zheng et al., 2008); the activities of MCSs in the North China Plain are the most frequent in June, July and August, and the formations occur mostly around noon (Ma et al., 2021a); under the influence of sea–land breeze, the MCSs in South China propagate offshore (inland) at night (in the daytime) (Bai et al., 2020; Zheng et al., 2008).

The initiation, development, and organization of MCSs are controlled and regulated by synoptic and mesoscale circulations. Lewis and Gray (2010) found that MCSs in Britain are mainly affected by three types of circulations and that the organization of MCSs is related to the interaction of perturbations at the upper level and warm advections at the lower level. Peters and Schumacher (2014) divided the circulations favorable for MCSs in the Great Plains of the United States into warm season-type and synoptic-type circulations. The synoptic-type MCSs tended to occur downstream of a progressive upper-level trough along a low-level potential temperature gradient with the warmest air to the south and southeast. Warm-season-type MCSs typically occurred within the right-entrance of a minimally to anticyclonically curved upper-level jet along a low-level potential temperature gradient with the warmest air to the southwest. Song et al. (2019) found that the favorable environments for MCSs over the Great Plains of the United States have frontal characteristics and enhanced low-level jets, while the unfavorable environments feature enhanced upper-level ridges. Sugimoto and Ueno (2010) found that MCSs over the eastern Tibetan Plateau mainly occurred under the condition of the eastward extension of the upper tropospheric anticyclone with the enhancement of near-surface low pressure in the western plateau. He et al. (2017) classified the circulation patterns over central East China into nine typical types based on the geopotential height fields at 850 hPa, and MCSs mainly occurred in the meridional circulations, which were associated with the Western North Pacific Subtropical High to the east and a low-pressure system to the west.

The aforementioned studies show that different synoptic circulations often lead to different environmental conditions, and the interactions of environmental conditions, topography, underlying surface and other factors are highly nonlinear, which makes it difficult to forecast the initiation and development of MCSs. Previous studies involving the MCS life cycle are still limited in terms of understanding its formation. At present, thanks to high spatial-temporal resolution satellite data, the development of an MCS

from initiation to formation can be accurately captured through backward tracking. The middle reaches of the Yangtze River Basin (YRB) are located in the transitional zone between the second-step terrain (mountains) and the plains over East China, with complicated orography and various underlying surfaces. The Mei-yu fronts are very active in this area, and their precipitation and convection have unique characteristics and complicated mechanisms (Fu et al., 2011b; Sun & Zhang, 2012; Zhang et al., 2014, 2020; Wang et al., 2021). In the present study, the MCSs over the middle reaches of the YRB are identified and tracked first, and then, the MCS initiation is detected through backward tracking. Next, the temporal-spatial distribution and features of the MCSs are investigated. Finally, the synoptic circulations in this region are objectively classified into different patterns to find the circulations and environmental conditions favorable for the initiation of an MCS. The remainder of this paper is organized as follows. Section 2 introduces the data and methodologies. Section 3 presents the statistics of MCSs, including the temporal-spatial distributions of initiation and apparent features during their life cycles. Section 4 presents the objective classification of circulations in the middle reaches of the YRB and examines the circulation patterns and environmental conditions favorable for MCS initiation. Finally, a summary is given in Section 5.

2 Data and methodology

2.1 Data and focused area

The brightness temperature (BT) at the 10.8 μm band of the Advanced Geosynchronous Radiation Imager onboard the Fengyun-4A (FY-4A) satellite is used to identify and track MCSs in the present study. The spatial resolution of FY-4A BT data is 4 km at nadir. The temporal resolution of regional observations over China and its surrounding area is ~5 min (Yang et al., 2017). The BT fields used in the present study are limited to the region (~15–45 °N and 75–135 °E) shown in Fig. 1a to ensure consistency in the dataset. The integrities of the dataset during the warm season (April–September) of 2018–2021 are 93.26%, 97.65%, 97.07%, and 98.05%, respectively, with an average integrity of 94.51%.

Considering that the mechanisms of the convection related to tropical cyclones (TCs) are different from those of extratropical convection (Bister, 2001; Hendricks & Montgomery, 2006; Rodgers et al., 1991), MCSs induced by TCs and circulations related to TCs are excluded using the TC best-track dataset provided by the China

Meteorological Administration, and the temporal resolution is 3 h (Lu et al., 2021; Ying et al., 2014).

The fifth-generation ECMWF (European Centre for Medium Range Forecasts) reanalysis (ERA5) data, with a temporal resolution of 1 h and a spatial resolution of 0.25° (Hersbach et al., 2020), are used in the classification and composite analysis of circulations. The construction of proximity soundings is mainly based on ERA5 data. However, considering the differences in the boundary layer variables between reanalysis and observed soundings (Gensini et al., 2014; King & Kennedy, 2019), correcting the boundary layer variables of the reanalysis sounding is necessary. Therefore, the present study uses the 1-h observations of automatic weather stations (AWSs) provided by the China Meteorological Administration to correct the surface level of the ERA5 data before constructing proximity soundings.

The middle reaches of the YRB are defined as the region covering 107–119 °E and 25–35 °N in the present study (Fig. 1a), and the orography (Fig. 1b) in this area is complicated. The western Hubei mountainous areas and western Hunan mountainous areas are located in the west, the Nan-Ling Mountains are in the south and the Wu-Yi Mountains are in the southeast. The North China Plain is in the northeastern part of this region. Three smaller plains are in the middle, namely, the Jiang-Han Plain, the Dong-Ting Lake Plain and the Po-Yang Lake Plain, with the Da-Bie Mountains, the Mu-Lian-Jiu Mountains and the Luo-Xiao Mountains distributed from north to south.

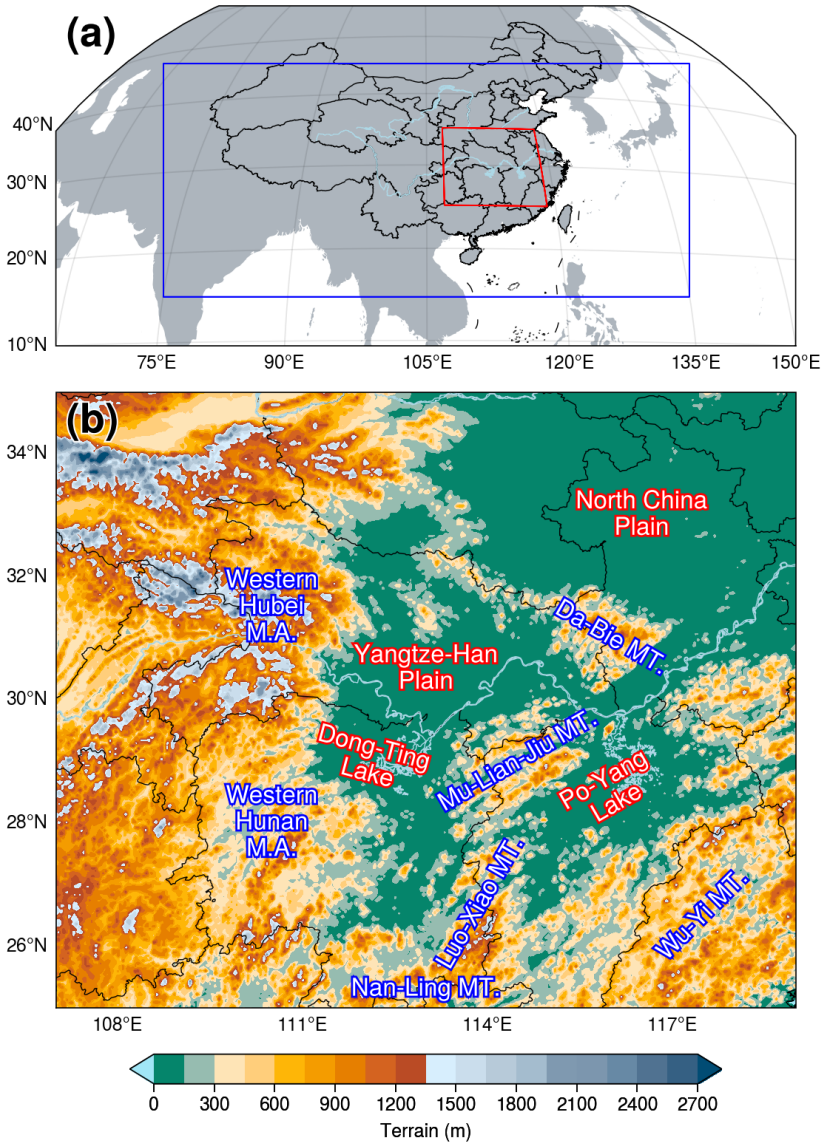

205

206 **Figure 1.** (a) The coverage of BT data (blue rectangle) in the present study and the
207 boundary of the middle reaches of the YRB (red line). (b) The terrain height (m) in the
208 middle reaches of the YRB. Mountains (MT.) and mountain areas (M.A.) are labeled in
209 blue, and plains and lakes are labeled in red.

210 2.2 Identifying and tracking methods

211 Following Yang et al. (2020), the criteria and steps used in the present study to
212 identify MCS are outlined as follows (Fig. 2): 1) detect CCSs with temperature ≤
213 −52 °C and extent ≥ 5000 km^2 in the BT fields; 2) track CCSs at different time steps;
214 and 3) continuous CCSs that last longer than 3 h are identified as MCSs. The first (last)
215 time that an MCS satisfies the above criteria is considered to be MCS formation
216 (termination). The time when the CCS of an MCS reaches its maximum extent is

considered to be MCS maturity.

The combination of areal overlap and optical flow is used in the present study to track CCSs with the following steps: 1) calculate the optical flow between two successive BT fields; 2) extrapolate the target CCS at the previous time by adding optical flow and compare it with the CCSs at the later time, and the one with an overlapping rate ≥ 30% is considered the successor of the target CCS; 3) if two CCSs or more satisfy the criterion of the areal overlapping rate at the later time, the one with the highest overlapping rate will be considered the successor of the target CCS; 4) examine the TC locations derived from the best-track dataset, and if there are any TC-related clouds within the coverage of a CCS, the CCS will be excluded because the CCS is a TC cloud instead of an MCS. Backward tracking is applied to find the initiation time and location of an MCS. Considering that the CCS is small and develops rapidly during the early stage of an MCS, no areal limitation has been applied during backward tracking.

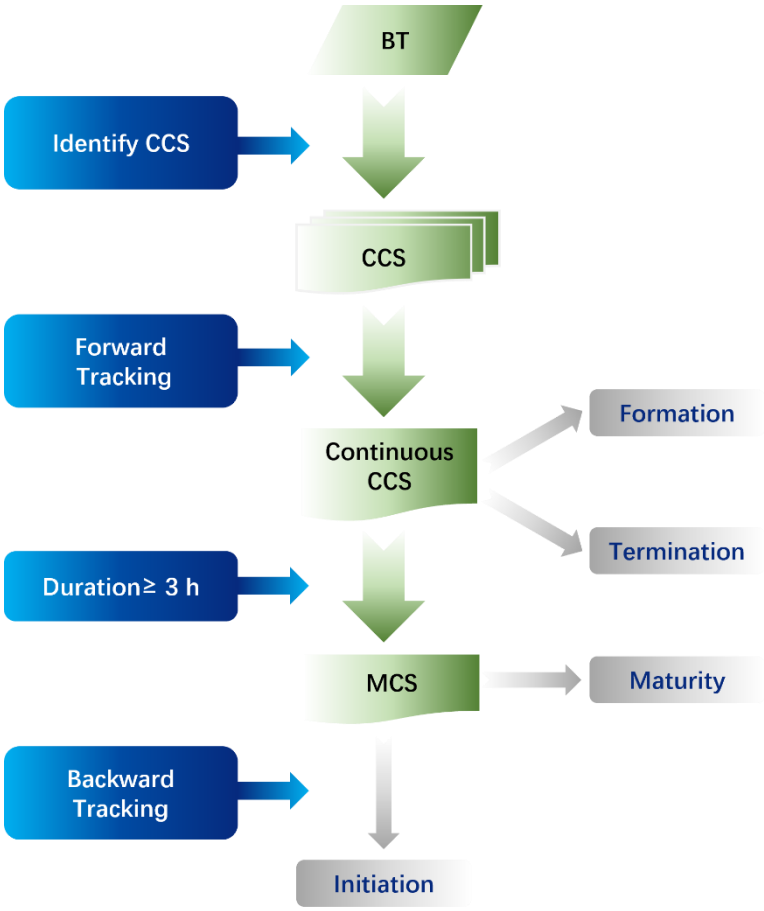

Figure 2. Flow chart of MCS identification and tracking.

2.3 Filtering of backward tracking

Backward tracking may not be accurate because the extent of a CCS is small and the motion is fast during the early stage of an MCS. The splitting and regeneration of MCSs, cirrus anvils, and deficiency of BT data may all lead to incorrect backward tracking. Therefore, further examinations are conducted on the backward tracking results. If two or more MCSs are initiated at the same time and location, it is considered that those MCSs are split from the same MCS or that one MCS is regenerated from another. Then, the initiation will be assigned to the earliest MCS according to the formation time, and the remaining MCSs will be regarded as inaccurate tracking and excluded from the MCS dataset. For the inaccurate backward tracking results caused by deficiency of BT data, the filtering approach is outlined as follows: check whether the BT data before the initiation time are missing; if true, the result will be regarded as inaccurate and excluded from the MCS dataset. CCSs connected with cirrus anvils are manually checked since they vary greatly between two successive times.

2.4 Objective classification

The *k-means* algorithm, which is widely used for classification in atmospheric research due to its stable performance (Hoffmann & Schlünzen, 2013; Huth et al., 2008; Kanungo et al., 2002; Ku et al., 2021; Solman & Menéndez, 2003; Stahl et al., 2006; Zhang et al., 1997), is applied in the present study for the objective classification of circulation patterns. The meteorological variable used for classification in the present study is the geopotential height field at 700 hPa. The geopotential height field is a commonly used variable in circulation classification (Hoffmann & Schlünzen, 2013; Liu et al., 2019; Miao et al., 2017; Ning et al., 2020; Yang et al., 2021). Huth et al. (2008) suggested that due to a high degree of dependence among individual levels, the inclusion of additional levels yields little extra information over using a single level, which has been confirmed in many studies (Dong et al., 2020; Liu et al., 2019; Miao et al., 2017; Ning et al., 2020; Yang et al., 2021). Statistics (see Section 3) in the present study suggest that MCSs are mainly initiated between 0300–0600 (Coordinated Universal Time, UTC) and that 78.4% (627 out of 800) of MCSs occur in June, July and August (JJA). In addition, circulation patterns vary greatly in September (Tao 1980). Therefore, the geopotential height fields at 700 hPa at 0000 UTC each day during JJA of 2018–2021 are used for circulation classification. TCs may have a great impact on synoptic circulations, leading to inaccurate classification results. Therefore,

based on the TC locations derived from best-track data, if a TC enters the area east of 124 °E and north of 20 °N on a certain day, this day will be recorded as a TC-day and will be excluded during circulation classification. A total of 83 TC days are excluded.

The silhouette coefficient (Rousseeuw, 1987) is calculated as an approach to evaluate the performance of different classification numbers. The silhouette coefficient considers both the homogeneity within a class and the difference between classes (Huth et al., 2008; Rousseeuw, 1987) and is widely used as criterion to determine the classification number (Bernard et al., 2013; Nga et al., 2021; Ternynck et al., 2016). The optimal choice of classification number in the present study is 3 based on the evaluation of the silhouette coefficient.

2.5 Construction of proximity soundings

Considering the coarse temporal-spatial resolutions of the observed radiosonde data, the environmental parameters in the present study are calculated from the reanalysis-derived proximity soundings based on ERA5 data. However, some previous studies have noted the differences in the boundary layer variables between reanalysis and observed soundings and that correcting the boundary layer variables of the reanalysis sounding is necessary (Gensini et al., 2014; King & Kennedy, 2019). Therefore, the hourly AWS observations are used to correct surface-level variables in ERA5 data before calculating environmental parameters.

The nearest hour before an MCS initiation and the ERA5 grid closest to the initiation are chosen as the time and location, respectively, to construct a proximity sounding. The closest AWS observation to the ERA5 grid within a radius of 100 km of the grid is selected to correct the surface-level variables of the ERA5 data. The ERA5 temperature/dew-point temperature profile is first constructed based on the isobaric layers (all 37 layers from 1000 hPa to 1 hPa). Then, the isobaric layers below the AWS surface pressure layer are neglected, and the AWS variables are deemed the lowest layer of the proximity sounding (Brooks et al., 2003; Ma et al., 2021b; Yang & Sun, 2018).

The environmental parameters are calculated based on proximity soundings to investigate the dynamic and thermodynamic conditions of MCS initiation under different circulation backgrounds. Ten parameters are selected, namely, the surface-based convective available potential energy (SBCAPE), the most unstable layer

convective available potential energy (MUCAPE), surface-based convective inhibition (SBCIN), most unstable layer convective inhibition (SBCIN), lifted index (LI), lifted condensation level (LCL), level of free convection (LFC), precipitable water (PW), 0–3 km bulk wind shear (SHR3) and 0–6 km bulk wind shear (SHR6). These parameters, with clear physical meanings and good performances in distinguishing between different intensities and types of convection, are widely used in convection environment studies (Brotzge et al., 2013; Grams et al., 2012; J. C. Kirkpatrick et al., 2007; Ma et al., 2021b; McCaul & Weisman, 2001; Yang & Sun, 2018).

3 Statistical characteristics

3.1 MCS trajectories and paths

On the one hand, the movements and propagations of MCSs are closely related to the occurrences of convective weather phenomena; on the other hand, they represent the regulation of large-scale circulations over mesoscale systems (Li et al., 2008; Yang et al., 2020; Jiang & Fan, 2002; Mai et al., 2020). In the present study, MCSs are categorized into quasistationary (QS) and outward-moving (OM) types. For QS MCSs, both the formations and terminations occur within the study area (Fig. 1b), and OM MCSs refer to those formed within the study area but terminated outside of the study area.

During the warm seasons (April–September) of 2018–2021, 800 MCSs are identified in the middle reaches of the YRB, where 524 are QS type and 276 are OM type, accounting for 65.5% and 34.5% of the total MCSs, respectively. Based on the movement trajectories of the MCSs, those of the QS type (Fig. 3a) are short and mainly within the study area. Part (13.7%) of the QS MCSs moved outside of the study area at certain times during their life cycles; however, they moved back into and terminated within the study area. The trajectories of OM MCSs (Fig. 3b) are longer than those of QS MCSs and are mainly eastward and southward. Most of the OM MCSs terminated after propagating into the oceanic area; however, some OM MCSs with long trajectories could reach the Pacific Ocean east of Japan or north of the Indo-China Peninsula.

To further investigate the main paths of the two types of MCSs, the *k-means* algorithm is adopted to classify MCS trajectories. Based on the evaluation of the silhouette coefficient, the trajectories of QS (OM) MCSs are classified into 4 (3) main paths. Among the 4 paths of the QS MCSs (Fig. 3c), the number of MCSs in the

southeast path is the largest, and the northwest path is the smallest. The lengths of the northeast and southeast paths are long, while those of the northwest and southwest paths are short. For the southeast and northeast paths, the average locations of MCS initiation are both located in the western Hunan mountainous area. For the southwest path and the northwest path, the average locations are in the western slope of the Mu-Lian-Jiu Mountains and the northern edge of the Luo-Xiao Mountains, respectively. Except for the northwest path with the smallest number of MCSs, the other 3 paths all move from the mountains to the plains. The phenomenon that convections are initiated in mountainous areas and propagate to the plains often occurs in the Rocky Mountains and the Great Plains of the United States (Carbone et al., 2002; Zhang et al., 2014) and the Tai-Hang Mountains and the North China Plain (He & Zhang, 2010; Zhu et al., 2018), which is related to the mountain-plain solenoid driven by thermodynamic effects (Bao et al., 2011; Sun & Zhang, 2012; Zhang & Sun, 2017). For the OM MCSs, among the 3 paths (Fig. 3d), the number of MCSs in the southeast path is the largest. The northeast path has the longest length, followed by the southeast path, and the southwest path has the shortest length. For the northeast path, the average location of MCS initiation is east of the Yangtze-Han Plain, and for the southeast path and the southwest path, the average locations are in the Mu-Lian-Jiu Mountains and the Luo-Xiao Mountains, respectively.

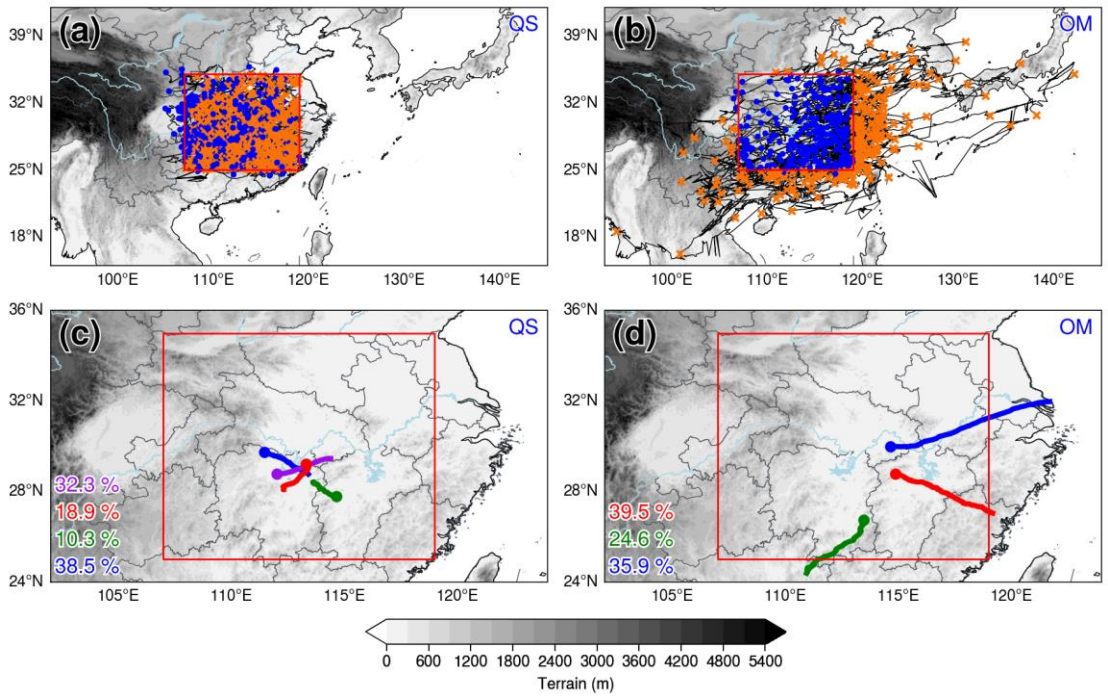

Figure 3. The movement trajectories of QS MCSs (a) and OM MCSs (b) and the composite movement paths of QS MCSs (c) and OM MCSs (d). The blue dots (orange crosses) in (a) and (b) represent the initiation (termination) locations of MCSs. Different paths are distinguished by different colors in (c) and (d), and the proportions of trajectories in different paths are marked in the lower left corner. The gray shading represents terrain height (m). The red rectangle indicates the boundary of the middle reaches of the YRB.

3.2 Temporal-spatial distribution of MCSs' initiations

The temporal distributions of MCS initiation are shown in Fig. 4. The QS MCSs mostly occur in July, followed by August (Fig. 4a), while the OM MCSs occur most frequently in July, followed by June (Fig. 4b). During the Mei-yu season in the YRB, namely, mid-June to mid-July (Tao, 1980), the mesoscale systems basically move eastward along the Mei-yu front. After mid-July, the convections in this area are mainly caused by local diabatic effects. These results explain why QS MCSs mostly occur in July and August, while OM MCSs mostly occur in June and July (Zhang et al., 2014). The QS MCSs are mainly (41.2%) initiated around noon (0400–0800 UTC), and the peak time is 0600–0700 UTC, which is identical in each month (Fig. 4a). However, the peak hours of initiation for OM MCSs vary in different months. In June and July, the initiation of OM MCSs has two peaks, one at noon (0300–0500 UTC) and the other at night (1800–1900 UTC). The noon peak is generally considered to be related to the instability caused by surface solar heating (Yu et al., 2007), and MCSs initiated during this time period correspond to the afternoon peak of summer precipitation in the YRB (Luo et al., 2016; Zhang et al., 2020). The mechanism for the late-night peak is complicated, which may result from instability due to nocturnal radiative cooling at the cloud top (Lin et al., 2000), water vapor accumulation at low levels in the evening (Kubota & Nitta, 2001), or diurnal variation in local circulation forced by complex terrain (He & Zhang, 2010; Li et al., 2005; Sun & Zhang, 2012; Zhang & Sun, 2017). Regardless of the triggering mechanism, the late-night initiation peak of the OM MCS corresponds to the morning peak of precipitation in the typical Mei-yu seasons (Luo et al., 2016; Zhang et al., 2020). In other months (except for September, which has only 4 MCSs), OM MCSs have only one peak in the afternoon (0600–0700 UTC), which is consistent with the QS type.

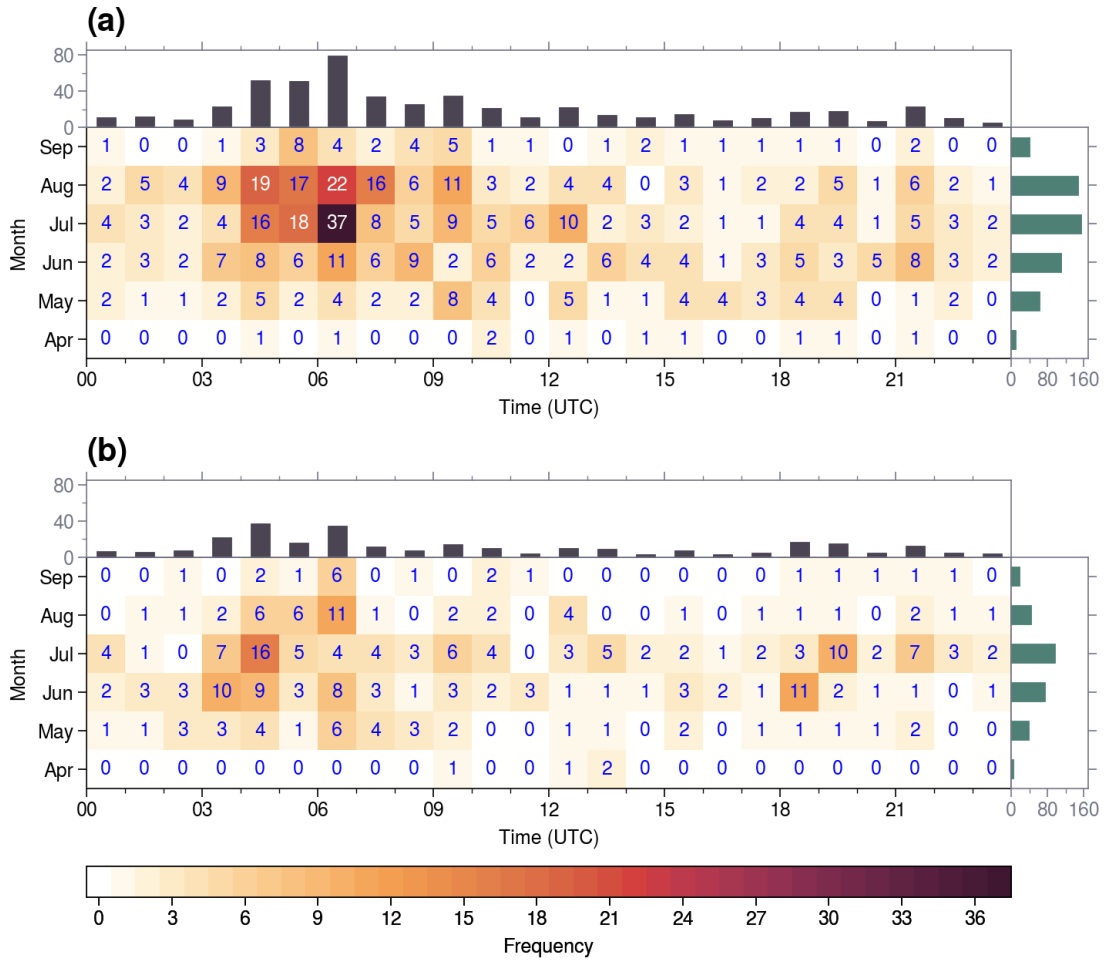

Figure 4. Monthly and diurnal distributions of the QS MCS frequency (a) and the OM MCS frequency (b) in the middle reaches of the YRB during the warm seasons (April–September) of 2018–2021. The horizontal axis represents the initiation time (UTC). The color shading symbolizes the occurrence frequency of MCSs.

The spatial distributions of MCS initiation are shown in Fig. 5. Both the QS MCSs (Fig. 5a) and the OM MCSs (Fig. 5b) are initiated mainly in the southern part of the YRB, which is consistent with a previous study (Zheng et al., 2008). Dividing the southern part of the YRB from the north roughly by 30 °N, 343 QS MCSs and 195 OM MCSs are initiated in the southern part of the YRB, accounting for 65.5% and 70.7% of their total amounts, respectively. The highest initiation frequency of QS MCSs is found over the western Hunan mountains, the Mu-Lian-Jiu Mountains and the Luo-Xiao Mountains, while that of the OM MCSs is over the Po-Yang Lake Plain. The convection in mountainous areas is mainly driven by the thermodynamic forcing (Astling, 1984; Panosetti et al., 2016; Zhu et al., 2018), while in plain areas, due to the

lack of dynamic forcing or diabatic heating resulting from the complex terrain, the initiation of convection is mostly related to synoptic circulation systems (Reif & Bluestein, 2017; Wilson & Roberts, 2006), which explains why QS MCSs are more likely to be initiated over mountainous areas, while OM MCSs tend to be initiated over plain areas.

To better illustrate the spatial distributions of MCS initiation, July and August (June and July) are chosen as the high occurrence period for QS (OM) MCSs. For QS MCSs, the spatial distribution of initiation in July and August (Fig. 5c) is basically the same as in the entire warm season (Fig. 5a), and the highest initiation frequency is also over the western Hunan mountains, the Mu-Lian-Jiu Mountains and the Luo-Xiao Mountains, with the highest probability density of 0.015 (0.014 for the entire warm season). This consistency further indicates that the initiation of QS MCSs in the middle reaches of the YRB is mainly caused by local thermodynamic effects and varies little in different months. For the OM MCSs, the spatial distribution of initiation in June and July (Fig. 5d) exhibits some differences compared with that of the entire warm season (Fig. 5b). Over the Po-Yang Lake Plain, the maximum probability density increases from 0.017 to 0.022, indicating that in June and July, OM MCSs are more likely to be initiated over the plain areas. In addition, the probability density contours extend from the maximum over Po-Yang Lake to the southwest along the Luo-Xiao Mountains and to the southeast along the Wu-Yi Mountains in the entire warm season, showing close relationships to orographic effects, but in June and July, the probability density contours show fewer extensions outward from the maximum center, indicating that the initiation of OM MCSs is less related to the terrain in June and July.

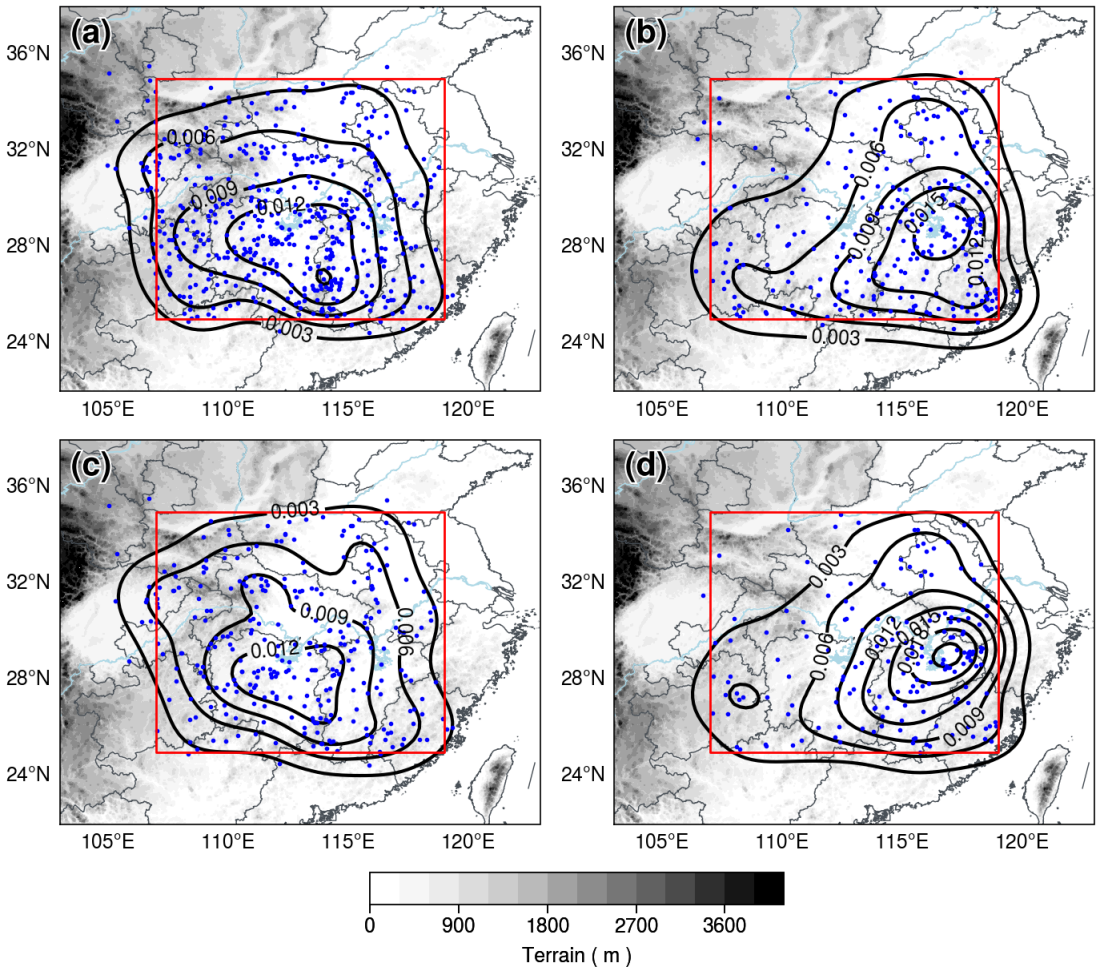

Figure 5. The spatial distribution of initiation locations of QS MCSs during the entire warm season (a) and in July and August (c) and OM MCSs during the entire warm season (b) and in June and July (d). The blue dots represent initiation locations, from which the spatial probability density is calculated and exhibited by the black contours. The red rectangle marks the middle reaches of the YRB. The gray shading represents terrain height (m).

3.3 Features of MCSs' movement

The moving velocity of an MCS between two consecutive times is calculated based on the centroid locations and the time interval. The average moving velocity of all times in the entire life cycle of an MCS is considered to be the bulk moving velocity of the MCS. In general, the speeds of OM MCSs are faster than those of QS MCSs (Fig. 6a). The movement of the MCS is regulated by the steering wind in the mid-lower troposphere (Rehbein et al., 2018); therefore, both the QS and OM MCSs move faster in April and May and slower in June, July and August. The speeds of the QS (OM)

MCSs are basically the same in July and August (June and July), indicating that the selection of a high occurrence period is reasonable. The speeds and directions of QS MCSs and OM MCSs in their high occurrence period are shown in Figs. 6 b and c. More than 80% of QS MCSs move at speeds of 0–45 km h^{-1}, and the highest proportion is located in the range of 15–30 km h^{-1}, accounting for 44% of all QS MCSs. Most (more than 70%) OM MCSs move at speeds of 15–60 km h^{-1}, with the highest proportion in the range of 30–45 km h^{-1}, accounting for 32%. The moving directions of the QS MCSs are relatively evenly distributed in all 8 directions in July and August with roughly similar proportions, which also indicates that the QS MCSs in July and August are less related to the activities of synoptic systems. The synoptic systems in the middle reaches of the YRB generally move eastward (Fu et al., 2011a; Zhang et al., 2018; Zhang & Sun, 2017), resulting in more than 50% of OM MCSs moving eastward and no OM MCS moving north or northwestward.

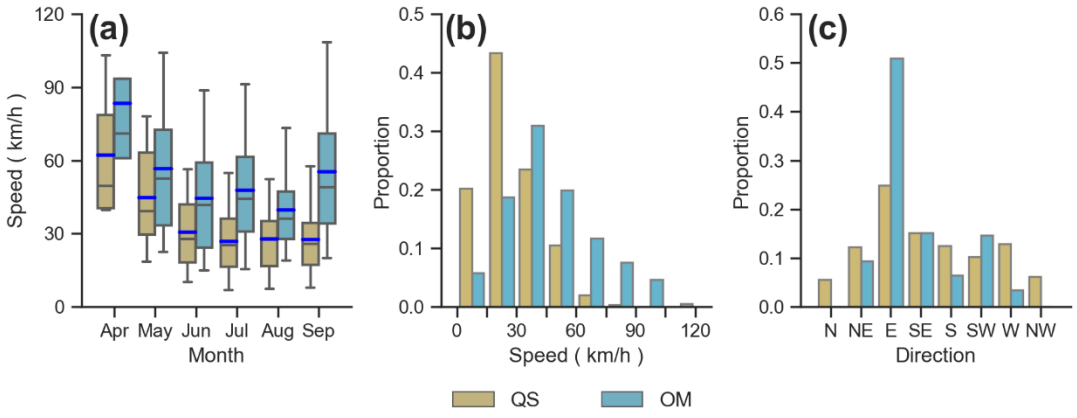

Figure 6. Box-and-whisker plot of MCS speed (a, km h^{-1}) during the warm seasons of 2018–2021 (a). The upper and lower edges (caps) of the boxes (whiskers) in the box-and-whisker plot represent the 3rd and 1st quartiles (95th and 5th percentiles), respectively. The black (blue) dashes inside boxes represent the medians (mean values). Histograms of MCS movement speeds (b, km h^{-1}) and directions (c) in the high occurrence period.

3.4 Duration, maximum extent and lowest temperature of MCSs

The duration and maximum extent represent the temporal-spatial scale of an MCS, and the lowest brightness temperature may reflect the intensity of the strongest convection in the MCS. In this section, box-and-whisker plots are applied to examine

459 the distributions of the three features in the entire warm season (Figs. 7 a, d and g).
460 Then, the proportion distributions (Figs. 7 b, e and h) and the pairwise relationships
461 (Figs. 7 c, f and i) of these features in the high occurrence period (July and August for
462 the QS MCSs and June and July for the OM MCSs) are analyzed.

463 Basically, the OM MCSs last longer than the QS MCSs (Fig. 7 a). The QS MCSs
464 mainly last for 5–10 h, with no significant variations between different months. The
465 OM MCSs in June last longer than those in other months, with an average duration of
466 ~20 h. The maximum extents of QS MCSs are mainly smaller than 5×10^4 km^2, while
467 those of OM MCSs are mostly between 2×10^4 km^2 and 1.5×10^5 km^2 and vary from
468 month to month. The lowest temperature shows a similar distribution between the QS
469 MCSs and the OM MCSs with an average value of approximately 190 K. The
470 mechanisms of initiation and development of QS MCSs are related to the local
471 thermodynamic effects, resulting in little difference in duration and maximum extent
472 between months. However, OM MCSs are mainly caused by synoptic systems that vary
473 in different months in the middle reaches of the YRB (Wang et al., 2021; Sun et al.,
474 2018), leading to complexity in the mechanisms of the initiation and development of
475 OM MCSs, further resulting in differences in duration and maximum extent between
476 months.

477 In July and August, nearly 40% of QS MCSs last 6–9 h and 30% last 3–6 h. In
478 June and July, more than 60% of OM MCSs last 6–15 h, with ~20% of each 3-h interval.
479 The maximum extents of QS MCSs in July and August are mainly 5×10^3–3×10^4 km^2,
480 accounting for more than 60%, while the maximum extents of the OM MCSs in June
481 and July are distributed evenly in the 5×10^3–3×10^4 km^2, 3×10^4–5.5×10^4 km^2 and
482 5.5×10^4–8×10^4 km^2 intervals, with each accounting for ~20%. For the lowest
483 temperature, half of the QS (OM) MCSs are 184–196 K (190–202 K) in July and
484 August (June and July).

485 Based on the above analysis, there are certain connections among the duration,
486 maximum extent and lowest temperature of MCSs. The pairwise correlations of the
487 three features in the high occurrence period are shown in Figs. 7 c, f and i. In general,
488 the longer the durations of the MCSs are, the larger the maximum extents and the colder
489 the cloud tops. With the extension of duration, the maximum extent shows an enlarging
490 trend (Fig. 7c), which is consistent between the QS type and the OM type. With the
491 increase in the maximum extent, the lowest temperature decreases (Fig. 7f), and that of

the QS type decreases faster than that of the OM type. With increasing duration, the lowest temperature shows a deceasing trend (Fig. 7i), and that of the QS MCSs also decreases faster.

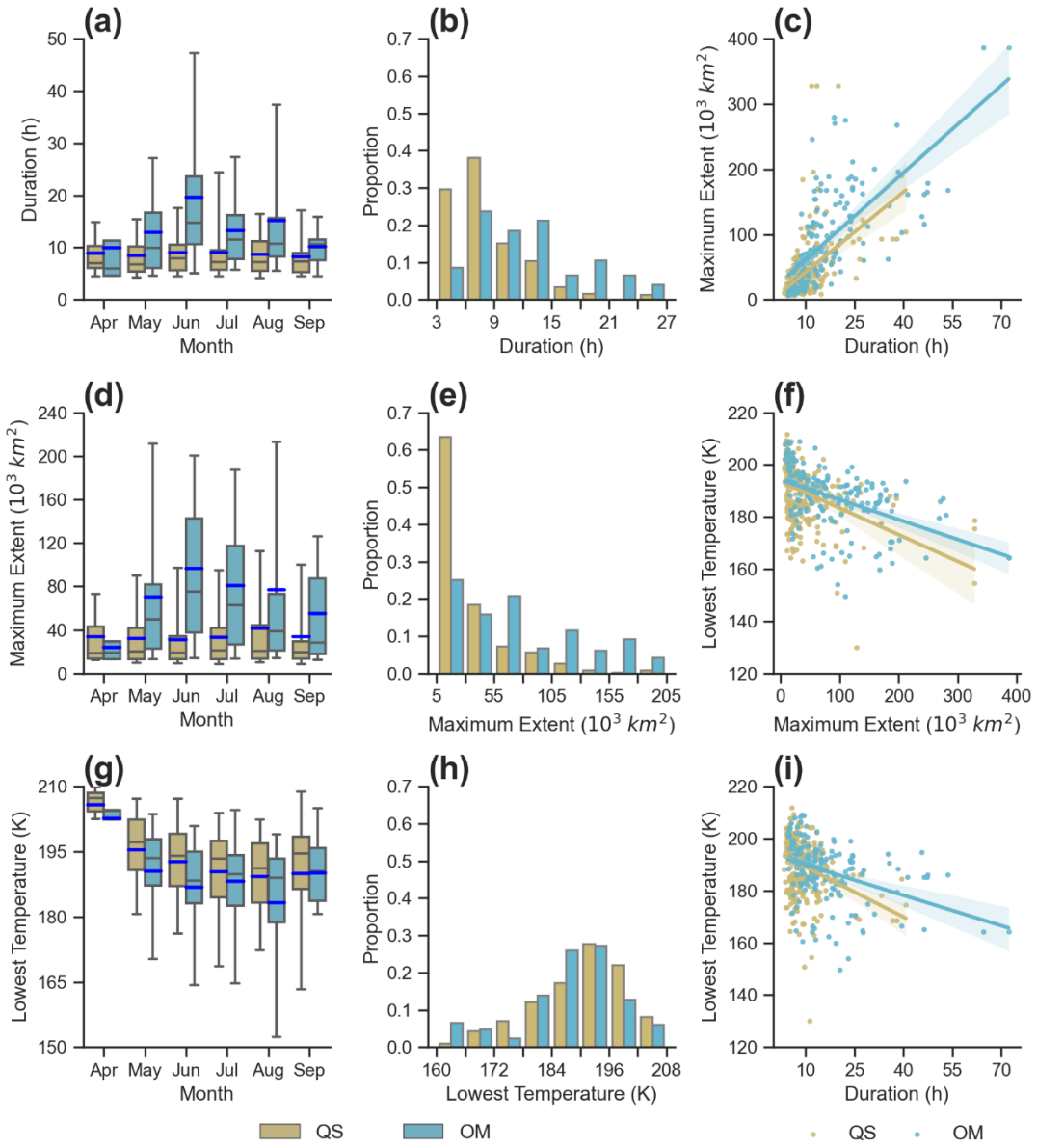

Figure 7. The box-and-whisker plots on the left are the duration (a), the maximum extent (d) and the lowest temperature (g) of MCSs during the entire warm seasons of 2018–2021. The upper and lower edges (caps) of the boxes (whiskers) in the box-and-whisker plot represent the 3rd and 1st quartiles (95th and 5th percentiles), respectively. The black (blue) dashes inside boxes represent the medians (mean values). The histograms of the central column are the proportion of the duration (b), the maximum extent (e) and the lowest temperature (h) of MCSs in high occurrence periods of 2018–

2021. The scatter plots on the right are the pairwise relationships between the duration and the maximum extent (c), the maximum extent and the lowest temperature (f), and the duration and the lowest temperature (i) in high occurrence periods of 2018–2021.

3.5 Diurnal variation in maximum extent and lowest temperature

To investigate the diurnal variation in the MCSs in the middle reaches of the YRB, the time when the maximum extent (lowest temperature) appears and the time span between MCS initiation and the maximum extent (lowest temperature) appearance are further examined. Since 58% of QS MCSs are initiated in July and August and 62% of OM MCSs occur in June and July, to highlight the difference between QS MCSs and OM MCSs, only MCSs in high occurrence periods are analyzed, and the results are shown in Fig. 8.

In July and August, the initiation frequency of QS MCSs peaks in the afternoon (0600–0700 UTC, Fig. 8a, upper subplot), which is the same as the result from the entire warm season (Fig. 3a). In June and July, the initiation frequency of OM MCSs has two peaks, namely, noon peak (0300–0500 UTC) and late-night peak (1800–2000 UTC, Fig. 8b, upper subplot). For the OM MCSs, compared with the result from the entire warm season (Fig. 3b), the proportions of MCS initiation during the noon peak (0300–0500 UTC) and the late-night peak (1800–2000 UTC) increase, but that during the afternoon peak (0600–0700 UTC) decreases.

In July and August, the lowest temperatures of QS MCSs mainly appear in the afternoon (0700–1100 UTC), with a peak at 0800–0900 UTC (Fig. 8a, the main plot and the subplot on the right-hand side). The surface solar heating is the strongest in the afternoon; therefore, convective activities are most vigorous during this time period. In June and July, the lowest temperatures of OM MCSs mainly appear in the afternoon and the evening, distributed evenly during this time period without any obvious peak (Fig. 8b, the main plot and the subplot on the right-hand side). As mentioned before, OM MCSs are mainly associated with synoptic circulation systems, and the mechanisms for convection development are complicated, resulting in no obvious peak for the lowest temperature appearance. In July and August, the maximum extents of QS MCSs mainly appear in the evening (0900–1200 UTC, Fig. 8c, the main plot and the subplot on the right-hand side), 1–2 h later than the appearance of the lowest temperature. In June and July, the maximum extents of OM MCSs mainly appear in the

evening (0900–1100 UTC) (Fig. 8d, the main plot and the subplot on the right-hand side).

In July and August, the lowest temperatures (the maximum extents) of the QS MCSs appear 4.43 h (6.03 h) after initiation. The QS MCSs initiated at noon or in the afternoon (0500–1000 UTC) reach the lowest temperature ~3 h after initiation (Fig. 8a, lower subplot), which indicates that the QS MCSs caused by local thermodynamic effects in this time period develop at roughly the same pace. The QS MCSs in July and August mainly achieve the maximum extent 4–7 h after initiation (Fig. 8c, lower subplot). In June and July, the lowest temperatures (maximum extents) of the OM MCSs appear 6.8 h (9.21 h) after initiation (lower subplots in Figs. 8 b and d). The development of OM MCSs is associated with many factors (i.e., synoptic systems, orography, and underlying surface) and interactions between these factors; therefore, the diurnal variations follow no obvious pattern.

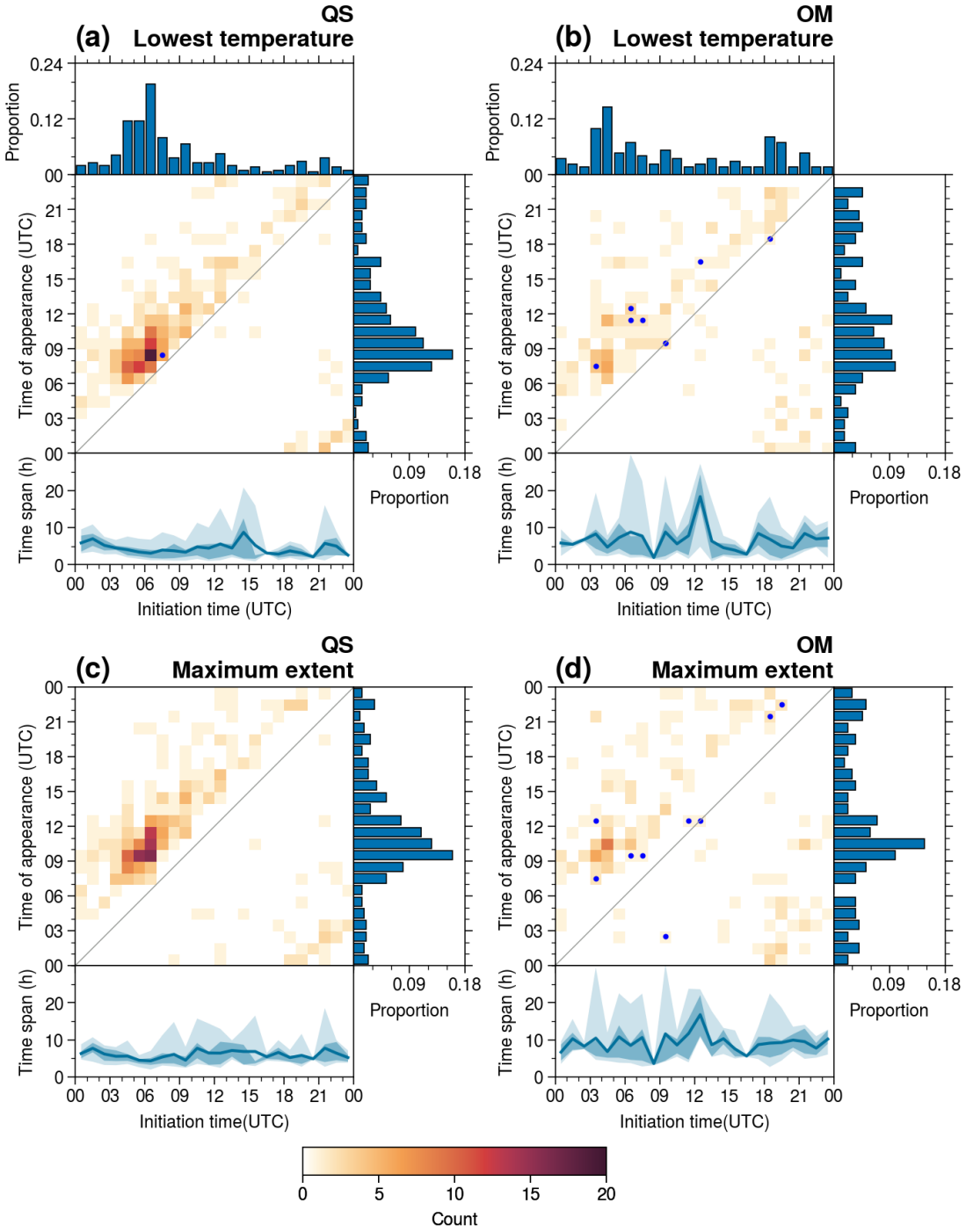

Figure 8. The two-dimensional histogram for the diurnal variation in the lowest temperature appearance of QS MCSs (a) and OM MCSs (b) and the maximum extent appearance of QS MCSs (c) and OM MCSs (d) in the high occurrence period of 2018–2021. The main body of each plot exhibits the frequency of MCS initiation and the lowest temperature (maximum extent) in every hourly interval. The upper histogram exhibits the proportion of MCS initiation. The left histogram exhibits the proportion of the lowest temperature (maximum extent) appearance. The lower plot exhibits the time

span between the lowest temperature (maximum extent) appearance and MCS initiation, with the solid line representing the mean time span and the light (dark) shading representing the 5%–95% (25%–75%) percentile interval. The blue dot indicates that the time span is longer than 24 h.

4 Circulation patterns and environmental conditions for MCS initiation

To investigate the circulation patterns favorable for MCS initiation, the daily circulations at 0000 UTC in JJA of 2018−2021 are objectively classified into 3 patterns by adopting the *k-means* algorithm, and the environmental parameters under different circulation patterns are further analyzed.

4.1 Objective classification of circulation patterns

Circulations of 285 days without direct influencings from tropical cyclones in JJA of 2018−2021 are classified into 3 patterns according to the evaluation based on the silhouette coefficient, with 128, 66 and 91 days in each pattern, respectively, and the composite fields of geopotential height at 700 hPa are shown in Fig. 9. Pattern-I (P1) is the typical circulation of the Mei-yu front (Fig. 9a). With a shallow trough in northeast China and the Indo-China Peninsula, the middle reaches of the YRB are in a large-scale convergence zone formed by the northwesterlies from the high latitudes and the southwesterlies from the low latitudes, which is consistent with the shear line and the strong equivalent potential temperature gradient. In Pattern-II (P2), the middle reaches of the YRB are basically under the control of the northwesterly, to the east of which is a deep trough (Fig. 9b). Although the equivalent potential temperature field also shows a strong gradient in P2, the thermodynamic characteristics of circulations in P1 and P2 are different. In P1, a warm humid air flow is dominated by the strong southwesterly, with a warm tongue extending from southwest to northeast. In P2, the northwesterly is the dominant wind, steering a cold tongue extending from north to south. The equivalent potential temperature field in P1 (336–348 K) is higher than that in P2 (332–340 K), indicating that the air mass in P1 is warmer or wetter than that in P2. In Pattern-III (P3), the middle reaches of the YRB are under the control of the weak southerly to the east of the Western Pacific Subtropical High.

A total of 330 QS MCSs and 187 OM MCSs are initiated during JJA of 2018–2021. Fifty percent of QS MCSs and 59.9% of OM MCSs are initiated in P1, suggesting that P1 is favorable for both QS and OM MCS initiation. Thirteen percent (36.1%) of

the QS MCSs and 25.7% (14.4%) of the OM MCSs are initiated in P2 (P3). The daily average initiation frequencies of QS MCSs in the three patterns are 1.31, 0.65 and 1.31, and those of the OM MCSs are 0.88, 0.72 and 0.3, respectively. In general, the QS MCS initiation in P1 and P3 is the same and in P2 is the least, while the OM MCSs are initiated the most in P1, followed by P2 and the least in P3.

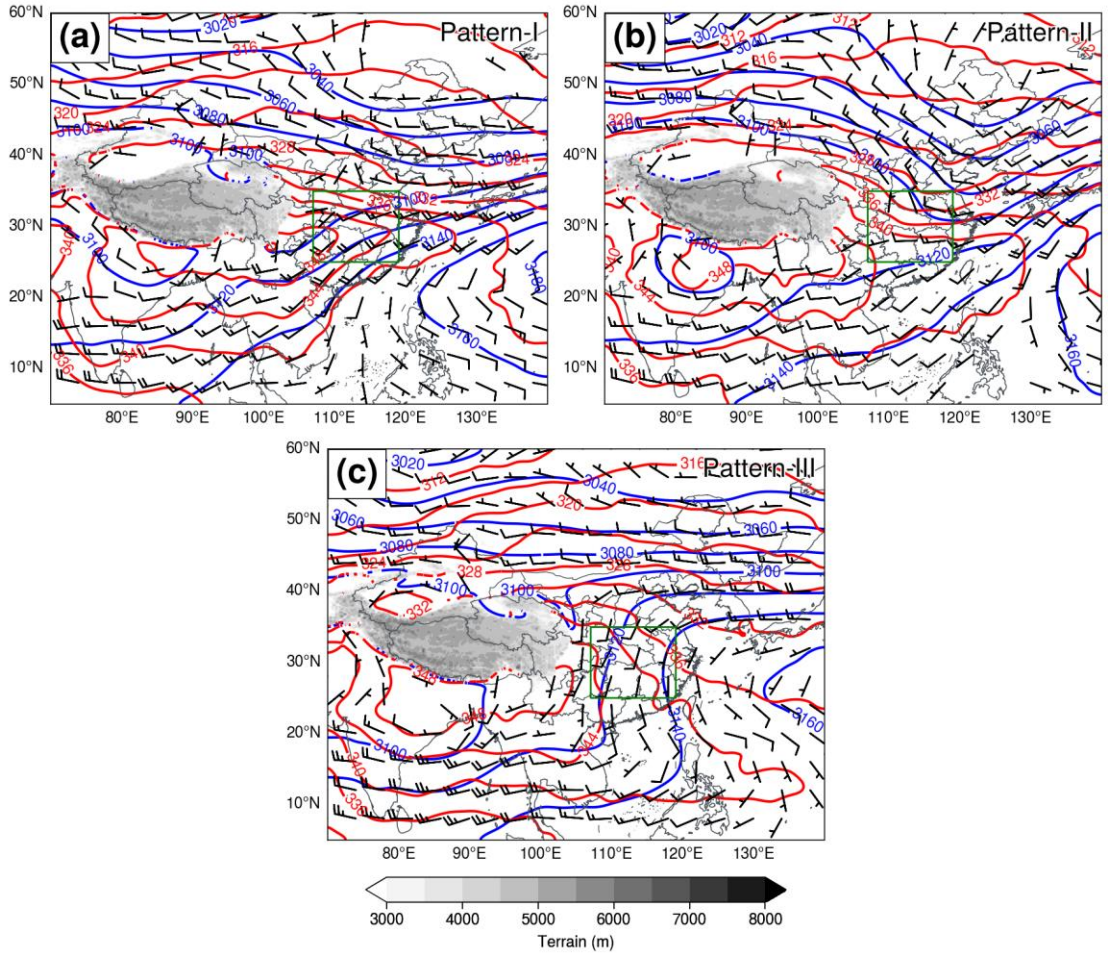

Figure 9. The composite geopotential fields (blue contours, gpm), equivalent potential temperature fields (red contours, K) and wind fields (wind barbs, m s^{-1}) at 700 hPa of Pattern-I (a), Pattern-II (b) and Pattern-III (c), respectively. A half (full) barb represents 2 m s^{-1} (4 m s^{-1}). The green rectangle marks the middle reaches of the YRB. The gray shading represents terrain heights (m).

4.2. Environmental parameters

To investigate the dynamic and thermodynamic conditions for MCS initiation under the three circulation patterns, ten environmental parameters are statistically

analyzed, and the results are shown in Fig. 10.

The mean value of SBCAPE in P1 (Fig. 10 a) is 2363 J kg^{-1} and that of MUCAPE is 2491 J kg^{-1}, both the lowest in the three patterns. A low CAPE often implies a high LFC height or a small environmental lapse rate, yet the LFC height in P1 is the lowest in the three patterns (Fig. 10g) with a mean value of 743 m, which suggests that the lapse rate of the mid-low troposphere in P1 is small. The mean value of LI in P1 (Fig. 10e) is −4.4 K, the highest in the three patterns, which also confirms this conclusion. The mean PW in P1 (Fig. 10h) is 65 mm, which is significantly higher than those in P2 and P3. The contribution to the local water vapor growth in the YRB often came from the southwesterly and southeasterly originating from the oceans (Li et al., 2014; Shi et al., 2020; Wang et al., 2021), which is consistent with the synoptic circulation in P1.

The mean SHR3 (Fig. 10i) and SHR6 (Fig. 10j) in P1 are 9 m s^{-1} and 8.9 m $s^{-1,}$ respectively, which are both significantly higher than those in P2 and P3. In P2 and P3, the SHR6s are basically 1 m s^{-1} higher than the SHR3s (both the median and mean value). However, in P1, the medians of SHR6 and SHR3 are basically equal, and the mean values of SHR6 are even lower than those of SHR3. There is little difference between SHR3 and SHR6 in P1, but the SHR6s in P2 and P3 are higher than the SHR3s, which suggests that the wind speed in the low troposphere in P1 is high or that MCS initiation in P1 may often be accompanied by low-level jets. Higher vertical wind shears in P1 may be the reason why OM MCSs tend to occur in P1 (Cohen et al., 2007).

The mean SBCAPE (MUCAPE) in P2 is 2366 J kg^{-1} (2650 J kg^{-1}). The difference between MUCAPE and SBCAPE in P2 is the largest among the three patterns, indicating that the atmosphere in the boundary layer in P2 is more stable than those in P1 and P3, which is consistent with the composite circulation in P2, dominated by northerlies. In operational forecasts, a stable boundary layer and a low CAPE can be misleading and cause the possible elevated convections to be ignored. The mean SBCIN in P2 is 30 J kg^{-1} (Fig. 10b), and the mean MUCIN in P2 is 11.9 J kg^{-1} (Fig. 10d), and both SBCIN and MUCIN were significantly higher than those in P1 and P3. In P2, 25% of MCSs are initiated in the environment with SBCIN greater than 34 J kg^{-1} (Fig. 10b). The large SBCIN in P2 confirms the aforementioned conclusion that the low-level atmosphere in P2 is more stable than those in P1 and P3. The mean LCL height in P2 (Fig. 10f) is 356 m, which is the lowest among the three patterns, and the mean LFC

height (Fig. 10g) is 864 m. The lowest LCL height in P2 indicates a high relative humidity at the surface, which may be caused by the cold invasion related to the northerly.

Both the mean SBCAPE (Fig. 10a) and the mean MUCAPE (Fig. 10c) in P3 are 3132 J kg^{-1} and are significantly higher than those in P1 and P2. More than 25% of MCSs are initiated in the environment with SBCAPE over 4000 J kg^{-1}. The mean PW in P3 (Fig. 10h) is 61 mm, the mean SHR3 (Fig. 10i) is 6.2 m s^{-1}, and the mean SHR6 (Fig. 10j) is 7.3 m s^{-1}. Although different environmental parameters are not simply compensated for each other (Kirkpatrick et al., 2007), considering the lack of synoptic forcing and the lowest PW (Fig. 10j) in P3, a higher CAPE may be required during MCS initiation (Kirkpatrick et al., 2009; McCaul & Weisman, 2001), and it is suggested that in an environment with a large CAPE, a higher LFC height and a lower PW are beneficial for updrafts (Kirkpatrick et al., 2011), which is similar to the configuration in P3. The mean LCL height (Fig. 10f) is 716 m and is significantly higher than those in P1 and P2. The highest LCL height in P3 suggests a relatively dry boundary layer (Rasmussen & Blanchard, 1998), causing stronger evaporation and colder outflow from the downdrafts (Kuchera & Parker, 2006) and further resulting in severe wind on the surface ground (Evans & Doswell, 2001; Kaltenböck et al., 2009). The difference between the mean LFC height and the mean LCL height is smallest in P3. A high LCL height suggests a dry low-level environment, and a low LFC height represents a large lapse rate, which indicates that the impact of the southerly in P3 is greater on warming than on humidification. This conclusion can also be confirmed by the lowest PW (Fig. 10h) in P3. The mean SBCIN (Fig. 10b) is 13 J $kg^{-1,}$ and the mean MUCIN (Fig. 10d) is 7.3 J kg^{-1}, and both are the minimum in the 3 patterns. Note that the medians of the SBCIN and the MUCIN in P3 are both 0 J kg^{-1}, which suggests that more than half of the MCSs in P3 are triggered in the environment with no CIN. However, the mean LFC height in P3 is the highest, combined with the minimum CIN, representing a dry-adiabatic or even superadiabatic low-level atmosphere, which confirms the conclusion that the southerly in P3 is more favorable for warming than for humidifying.

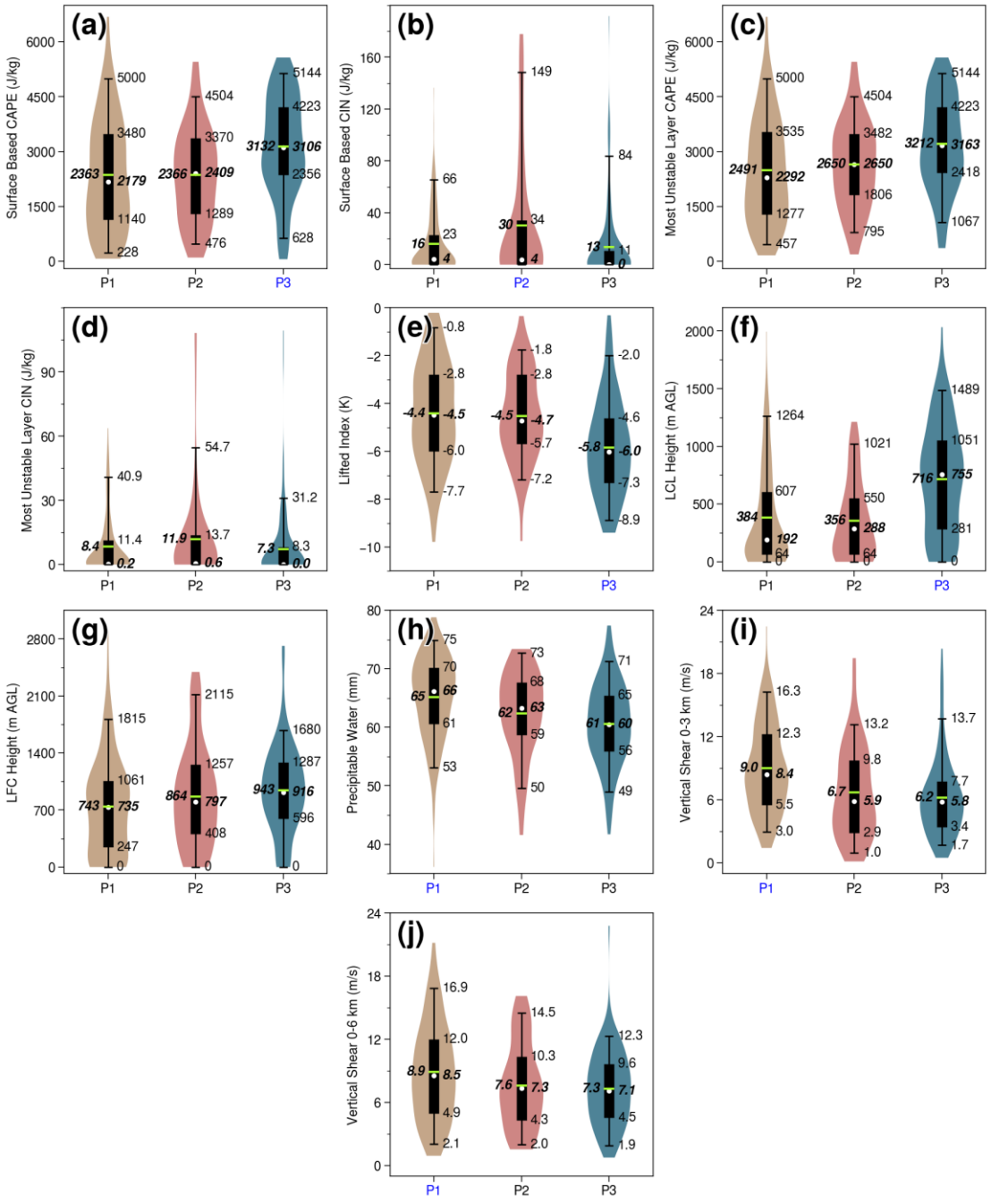

668

669 **Figure 10.** Violin plots of environmental parameters. From (a) to (j) are SBCAPE (J
670 kg^{-1}), SBCIN (J kg^{-1}), MUCAPE (J kg^{-1}), MUCIN (J kg^{-1}), LI (K), LCL (m), LFC (m),
671 PW (mm), SHR3 (m s^{-1}), and SHR6 (m s^{-1}). The outline of the violin represents the
672 probability density. The upper and lower edges (caps) of the box (whiskers) inside the
673 violin represent the 3rd and 1st quartiles (95th and 5th percentiles), respectively, which
674 are marked on the right side of the violin. The white dot (lemon dash) inside the box
675 represents the median (mean value), which is marked in bold italics on the right (left).
676 The pattern label marked blue indicates that the mean value of the parameter in this

pattern is significantly (above the 95% level based on a two-tailed Welch's *t* test) different from those in the other two patterns.

5 Summary and conclusions

Based on the BT data from the Advanced Geosynchronous Radiation Imager onboard the FY-4A satellite during the warm seasons (April–September) of 2018–2021, the combination of areal overlapping and optical flow is adopted to identify and track the MCSs in the middle reaches of the YRB, which are categorized into the quasistationary (QS) type and the outward-moving (OM) type and are statistically analyzed. The daily circulations of JJA, during which MCSs occur most frequently, are objectively classified into three patterns using the *k-means* algorithm, and the environmental conditions of MCS initiation are further compared and analyzed. The main conclusions are described as follows:

(1) During the warm seasons of 2018–2021, 524 QS MCSs and 276 OM MCSs are identified in the middle reaches of the YRB. Among the four main moving paths (i.e., northeast path, southeast path, northwest path and southwest path) of QS MCSs, the occurrence frequency in the southeast path is the highest. The QS MCSs are mostly initiated over mountainous areas and then propagate to the plains. The moving trajectories of OM MCSs are classified into three paths, namely, the northeast path, the southeast path and the southwest path, among which the southeast path has the largest amount of OM MCSs.

(2) The QS MCSs primarily occur in July and August and are mainly initiated in the afternoon (0600–0700 UTC). The OM MCSs mostly occur in June and July with two initiation peaks at noon (0300–0500 UTC) and late night (1800–1900 UTC), respectively, corresponding to the afternoon peak and morning peak of the typical precipitation associated with Mei-yu fronts. QS MCSs are mainly initiated in mountainous areas and caused by local thermal effects, while OM MCSs are mostly triggered in plain areas, which is related to synoptic circulation forcings.

(3) The OM MCSs move faster than the QS MCSs and mostly propagate eastward. The durations and maximum extents of QS MCSs show no obvious differences among different months, while those of OM MCSs vary among different months. The lowest brightness temperatures of QS MCSs mostly appear in the afternoon (0800–0900 UTC), but those of the OM MCSs exhibit no obvious diurnal

variation.

(4) Circulations at 0000 UTC of 285 MCS days, without direct influencings from tropical cyclones, are classified into 3 patterns using the k-means algorithm. The composite circulation of P1 is consistent with the typical circulation of the Mei-yu front, and those of P2 and P3 are dominated by the northwesterly and the weak southerly, respectively. The mean initiation frequencies of the QS MCSs in P1 and P3 are the same and that in P2 is the lowest. The OM MCSs are initiated the most in P1, followed by P2, and they are initiated the least in P3.

(5) Analysis of the environmental conditions favorable for MCS initiation in the three circulation patterns suggests that a) the low-level wind speed in P1 is relatively high, and the MCS initiations in P1 may be accompanied by low-level jets, which is more favorable for OM MCS initiation and propagation; b) the circulation in P2 is dominated by northwesterlies with a relatively stable layer in the low-level troposphere; and c) the southerly in P3 accompanied by adiabatic warming establishes a dry-adiabatic or even a superadiabatic layer and further lowers the stability.

In the present work, a comprehensive analysis was conducted on the MCSs in the middle reaches of the YRB during the warm seasons of 2018–2021, focusing mainly on the statistical characteristics, circulation patterns, and environmental conditions favorable for MCS initiation, and some conclusions with scientific significance and utility value were obtained. However, some problems remain unsolved. For example, the late-night triggering peak of OM MCSs is not well understood, and the impacts of orography on MCSs in the middle reaches of the YRB need further exploration. Further work will focus on these issues.

Acknowledgments

This research was supported by the National Natural Science Foundation of China (Grant U2142202, 41975056 and 41975057).

Data Availability Statement

The FY-4A BT data can be downloaded from http://data.cma.cn/ with approval of China Meteorological Administration. The ERA5 dataset can be downloaded freely from https://cds.climate.copernicus.eu/cdsapp#!/home. The TC best-track dataset can be downloaded freely from https://tcdata.typhoon.org.cn/ zjljsjj_zlhq.html.

References

Astling, E. G. (1984). On the relationship between diurnal mesoscale circulations and precipitation in a mountain valley. *Journal of Applied Meteorology and Climatology*, *23*(12), 1635–1644. https://doi.org/10.1175/1520-0450(1984)023<1635:OTRBDM>2.0.CO;2

Augustine, J. A., & Howard, K. W. (1988). Mesoscale convective complexes over the United States during 1985. *Monthly Weather Review*, *116*(3), 685–701. https://doi.org/10.1175/1520-0493(1988)116<0685:MCCOTU>2.0.CO;2

Bai, L., Chen, G., & Huang, L. (2020). Convection initiation in monsoon coastal areas (South China). *Geophysical Research Letters*, *47*(11), e2020GL087035. https://doi.org/10.1029/2020GL087035

Bao, X., Zhang, F., & Sun, J. (2011). Diurnal variations of warm-season precipitation east of the Tibetan Plateau over China. *Monthly Weather Review*, *139*(9), 2790–2810. https://doi.org/10.1175/MWR-D-11-00006.1

Bechini, R., & Chandrasekar, V. (2017). An enhanced optical flow technique for radar nowcasting of precipitation and winds. *Journal of Atmospheric and Oceanic Technology*, *34*(12), 2637–2658. https://doi.org/10.1175/JTECH-D-17-0110.1

Bernard, E., Naveau, P., Vrac, M., & Mestre, O. (2013). Clustering of maxima: spatial dependencies among heavy rainfall in France. *Journal of Climate*, *26*(20), 7929–7937. https://doi.org/10.1175/JCLI-D-12-00836.1

Bister, M. (2001). Effect of peripheral convection on tropical cyclone formation. *Journal of the Atmospheric Sciences*, *58*(22), 3463–3476. https://doi.org/10.1175/1520-0469(2001)058<3463:EOPCOT>2.0.CO;2

Bowler, N. E. H., Pierce, C. E., & Seed, A. (2004). Development of a precipitation nowcasting algorithm based upon optical flow techniques. *Journal of Hydrology*, *288*(1–2), 74–91. https://doi.org/10.1016/j.jhydrol.2003.11.011

Brooks, H. E., Lee, J. W., & Craven, J. P. (2003). The spatial distribution of severe thunderstorm and tornado environments from global reanalysis data. *Atmospheric*

Research, *67–68*, 73–94. https://doi.org/10.1016/S0169-8095(03)00045-0

Brotzge, J. A., Nelson, S. E., Thompson, R. L., & Smith, B. T. (2013). Tornado probability of detection and lead time as a function of convective mode and environmental parameters. *Weather and Forecasting*, *28*(5), 1261–1276. https://doi.org/10.1175/WAF-D-12-00119.1

Burton, R. R., Blyth, A. M., Cui, Z., Groves, J., Lamptey, B. L., Fletcher, J. K., Marsham, J.H., Parker, D.J. & Roberts, A. (2022). Satellite-based nowcasting of west African mesoscale storms has skill at up to 4-h lead time. *Weather and Forecasting*, *37*(4), 445–455. https://doi.org/10.1175/WAF-D-21-0051.1

Carbone, R. E., Tuttle, J. D., Ahijevych, D. A., & Trier, S. B. (2002). Inferences of predictability associated with warm season precipitation episodes. *Journal of the Atmospheric Sciences*, *59*(13), 2033–2056. https://doi.org/10.1175/1520-0469(2002)059<2033:IOPAWW>2.0.CO;2

Cohen, A. E., Coniglio, M. C., Corfidi, S. F., & Corfidi, S. J. (2007). Discrimination of mesoscale convective system environments using sounding observations. *Weather and Forecasting*, *22*(5), 1045–1062. https://doi.org/10.1175/WAF1040.1

Dong, Y., Li, J., Guo, J., Jiang, Z., Chu, Y., Chang, L., Yang, Y. & Liao, H. (2020). The impact of synoptic patterns on summertime ozone pollution in the North China Plain. *Science of The Total Environment*, *735*, 139559. https://doi.org/10.1016/j.scitotenv.2020.139559

Evans, J. S., & Doswell, C. A. (2001). Examination of derecho environments using proximity soundings. *Weather and Forecasting*, *16*(3), 329–342. https://doi.org/10.1175/1520-0434(2001)016<0329:EODEUP>2.0.CO;2

Feng, Z., Leung, L. R., Houze, R. A., Hagos, S., Hardin, J., Yang, Q., Han, B. & Fan, J. (2018). Structure and evolution of mesoscale convective systems: sensitivity to cloud microphysics in convection-permitting simulations over the United States. *Journal of Advances in Modeling Earth Systems*, *10*(7), 1470–1494. https://doi.org/10.1029/2018MS001305

Feng, Z., Houze, R. A., Leung, L. R., Song, F., Hardin, J. C., Wang, J., Gustafson, W. I.

& Homeyer, C. R. (2019). Spatiotemporal characteristics and large-scale environments of mesoscale convective systems east of the Rocky Mountains. *Journal of Climate*, *32*(21), 7303–7328. https://doi.org/10.1175/JCLI-D-19-0137.1

Fu, S., Sun, J., Zhao, S., & Li, W. (2011a). The energy budget of a southwest vortex with heavy rainfall over south China. *Advances in Atmospheric Sciences*, *28*(3), 709–724. https://doi.org/10.1007/s00376-010-0026-z

Fu, S., Sun, J., Zhao, S., Li, W. & Li, B. (2011b). A study of the impacts of the eastward propagation of convective cloud systems over the Tibetan Plateau on the rainfall of the Yangtze-Huai River basin. *Acta Meteorologica Sinica*, *69*(4), 581–600, http://doi.org/10.11676/qxxb2011.051. (in Chinese)

Gallus, W. A., Snook, N. A., & Johnson, E. V. (2008). Spring and summer severe weather reports over the Midwest as a function of convective mode: a preliminary study. *Weather and Forecasting*, *23*(1), 101–113. https://doi.org/10.1175/2007WAF2006120.1

Gensini, V. A., Mote, T. L., & Brooks, H. E. (2014). Severe-thunderstorm reanalysis environments and collocated radiosonde observations. *Journal of Applied Meteorology and Climatology*, *53*(3), 742–751. https://doi.org/10.1175/JAMC-D-13-0263.1

Grams, J. S., Thompson, R. L., Snively, D. V., Prentice, J. A., Hodges, G. M., & Reames, L. J. (2012). A climatology and comparison of parameters for significant tornado events in the United States. *Weather and Forecasting*, *27*(1), 106–123. https://doi.org/10.1175/WAF-D-11-00008.1

He, H., & Zhang, F. (2010). Diurnal variations of warm-season precipitation over northern China. *Monthly Weather Review*, *138*(4), 1017–1025. https://doi.org/10.1175/2010MWR3356.1

He, Z., Zhang, Q., Bai, L., & Meng, Z. (2017). Characteristics of mesoscale convective systems in central East China and their reliance on atmospheric circulation patterns. *International Journal of Climatology*, *37*(7), 3276–3290. https://doi.org/10.1002/joc.4917

826 Hendricks, E. A., & Montgomery, M. T. (2006). Rapid scan views of convectively
827 generated mesovortices in sheared tropical cyclone Gustav (2002). *Weather and*
828 *Forecasting*, *21*(6), 1041–1050. https://doi.org/10.1175/WAF950.1

829 Hersbach, H., Bell, B., Berrisford, P., Hirahara, S., Horányi, A., Muñoz-Sabater, J., et
830 al. (2020). The ERA5 global reanalysis. *Quarterly Journal of the Royal*
831 *Meteorological Society*, *146*(730), 1999–2049. https://doi.org/10.1002/qj.3803

832 Hoffmann, P., & Schlünzen, K. H. (2013). Weather pattern classification to represent
833 the urban heat island in present and future climate. *Journal of Applied Meteorology*
834 *and Climatology*, *52*(12), 2699–2714. https://doi.org/10.1175/JAMC-D-12-065.1

835 Houze, R. A. (2004). Mesoscale convective systems. *Reviews of Geophysics*, *42*(4).
836 https://doi.org/10.1029/2004RG000150

837 Huth, R., Beck, C., Philipp, A., Demuzere, M., Ustrnul, Z., Cahynová, M., et al. (2008).
838 Classifications of atmospheric circulation patterns. *Annals of the New York*
839 *Academy of Sciences*, *1146*(1), 105–152. https://doi.org/10.1196/annals.1446.019

840 Jiang, J. & Fan, M. (2022). Convective clouds and mesoscale convective systems over
841 the Tibetan Plateau in summer. *Chinese Journal of Atmospheric Sciences*, *26*(2),
842 263–270, http://doi.org/10.3878/j.issn.1006-9895.2002.02.12. (in Chinese)

843 Kaltenböck, R., Diendorfer, G., & Dotzek, N. (2009). Evaluation of thunderstorm
844 indices from ECMWF analyses, lightning data and severe storm reports.
845 *Atmospheric Research*, *93*(1), 381–396. https://doi.org/10.1016/
846 j.atmosres.2008.11.005

847 Kanungo, T., Mount, D. M., Netanyahu, N. S., Piatko, C. D., Silverman, R., & Wu, A.
848 Y. (2002). An efficient k-means clustering algorithm: analysis and implementation.
849 *IEEE Transactions on Pattern Analysis and Machine Intelligence*, *24*(7), 881–892.
850 https://doi.org/10.1109/TPAMI.2002.1017616

851 King, A. T., & Kennedy, A. D. (2019). North American supercell environments in
852 atmospheric reanalyses and RUC-2. *Journal of Applied Meteorology and*
853 *Climatology*, *58*(1), 71–92. https://doi.org/10.1175/JAMC-D-18-0015.1

Kirkpatrick, J. C., McCaul, E. W., & Cohen, C. (2007). The motion of simulated convective storms as a function of basic environmental parameters. *Monthly Weather Review*, *135*(9), 3033–3051. https://doi.org/10.1175/MWR3447.1

Kirkpatrick, J. C., McCaul, E. W., & Cohen, C. (2009). Variability of updraft and downdraft characteristics in a large parameter space study of convective storms. *Monthly Weather Review*, *137*(5), 1550–1561. https://doi.org/10.1175/2008MWR2703.1

Kirkpatrick, J. C., McCaul, E. W., & Cohen, C. (2011). Sensitivities of simulated convective storms to environmental CAPE. *Monthly Weather Review*, *139*(11), 3514–3532. https://doi.org/10.1175/2011MWR3631.1

Kolios, S., & Feidas, H. (2010). A warm season climatology of mesoscale convective systems in the Mediterranean basin using satellite data. *Theoretical and Applied Climatology*, *102*(1–2), 29–42. https://doi.org/10.1007/s00704-009-0241-7

Ku, H.-Y., Noh, N., Jeong, J.-H., Koo, J.-H., Choi, W., Kim, B.-M., et al. (2021). Classification of large-scale circulation patterns and their spatio-temporal variability during High-PM10 events over the Korean Peninsula. *Atmospheric Environment*, *262*, 118632. https://doi.org/10.1016/j.atmosenv.2021.118632

Kubota, H., & Nitta, T. (2001). Diurnal variations of tropical convection observed during the TOGA-COARE. *Journal of the Meteorological Society of Japan. Ser. II*, *79*(3), 815–830. https://doi.org/10.2151/jmsj.79.815

Kuchera, E. L., & Parker, M. D. (2006). Severe convective wind rnvironments. *Weather and Forecasting*, *21*(4), 595–612. https://doi.org/10.1175/WAF931.1

Kukulies, J., Chen, D., & Curio, J. (2021). The role of mesoscale convective systems in precipitation in the Tibetan Plateau region. *Journal of Geophysical Research: Atmospheres*, *126*(23), e2021JD035279. https://doi.org/10.1029/2021JD035279

Laing, A. G., & Michael Fritsch, J. (1997). The global population of mesoscale convective complexes. *Quarterly Journal of the Royal Meteorological Society*, *123*(538), 389–405. https://doi.org/10.1002/qj.49712353807

Lewis, M. W., & Gray, S. L. (2010). Categorisation of synoptic environments associated with mesoscale convective systems over the UK. *Atmospheric Research*, *97*(1–2), 194–213. https://doi.org/10.1016/j.atmosres.2010.04.001

Li, J., Yu, R., Zhou, T., & Wang, B. (2005). Why is there an early spring cooling shift downstream of the Tibetan Plateau? *Journal of Climate*, *18*(22), 4660–4668. https://doi.org/10.1175/JCLI3568.1

Li, X., Zhou, W., Chen, D., Li, C., & Song, J. (2014). Water vapor transport and moisture budget over eastern China: remote forcing from the two types of El Niño. *Journal of Climate*, *27*(23), 8778–8792. https://doi.org/10.1175/JCLI-D-14-00049.1

Li, Y., Wang, Y., Yang, S., Hu, L., Gao, S., & Fu, R. (2008). Characteristics of summer convective systems initiated over the Tibetan Plateau. Part I: origin, track, development, and precipitation. *Journal of Applied Meteorology and Climatology*, *47*(10), 2679–2695. https://doi.org/10.1175/2008JAMC1695.1

Lin, X., Randall, D. A., & Fowler, L. D. (2000). Diurnal variability of the hydrologic cycle and radiative fluxes: comparisons between observations and a GCM. *Journal of Climate*, *13*(23), 4159–4179. https://doi.org/10.1175/1520-0442(2000)013<4159:DVOTHC>2.0.CO;2

Liu, N., Zhou, S., Liu, C., & Guo, J. (2019). Synoptic circulation pattern and boundary layer structure associated with PM2.5 during wintertime haze pollution episodes in Shanghai. *Atmospheric Research*, *228*, 186–195. https://doi.org/10.1016/j.atmosres.2019.06.001

Lu, X., Yu, H., Ying, M., Zhao, B., Zhang, S., Lin, L., et al. (2021). Western North Pacific tropical cyclone database created by the China Meteorological Administration. *Advances in Atmospheric Sciences*, *38*(4), 690–699. https://doi.org/10.1007/s00376-020-0211-7

Luo, Y., Wu, M., Ren, F., Li, J., & Wong, W.-K. (2016). Synoptic situations of extreme hourly precipitation over China. *Journal of Climate*, *29*(24), 8703–8719. https://doi.org/10.1175/JCLI-D-16-0057.1

911 Ma, R., Sun, J., & Yang, X. (2021a). A 7-yr climatology of the initiation, decay, and
912 morphology of severe convective storms during the warm season over North China.
913 *Monthly Weather Review*, *149*(8), 2599–2612. https://doi.org/10.1175/MWR-D-20-
914 0087.1

915 Ma, R., Sun, J., & Yang, X. (2021b). An eight-year climatology of the warm-season
916 severe thunderstorm environments over North China. *Atmospheric Research*, *254*,
917 105519. https://doi.org/10.1016/j.atmosres.2021.105519

918 Machado, L. A. T., Rossow, W. B., Guedes, R. L., & Walker, A. W. (1998). Life cycle
919 variations of mesoscale convective systems over the Americas. *Monthly Weather*
920 *Review*, *126*(6), 1630–1654. https://doi.org/10.1175/1520-0493(1998)126<1630:
921 LCVOMC>2.0.CO;2

922 Maddox, R. A. (1980). Mesoscale convective complexes. *Bulletin of the American*
923 *Meteorological Society*, *61*(11), 1374–1400. https://doi.org/10.1175/1520-
924 0477(1980)061<1374:MCC>2.0.CO;2

925 Mai Z., Fu, S., & Sun, J. (2020). Statistical features of two types of mesoscale
926 convective systems (MCSs) generated over the eastern Tibetan Plateau during 16
927 consecutive warm seasons. *Climatic and Environmental Research*, *25*(4), 385–398,
928 http://doi.org/10.3878/j.issn.1006-9585.2019.19040. (in Chinese)

929 Marzban, C., & Sandgathe, S. (2010). Optical flow for verification. *Weather and*
930 *Forecasting*, *25*(5), 1479–1494. https://doi.org/10.1175/2010WAF2222351.1

931 McCaul, E. W., & Weisman, M. L. (2001). The sensitivity of simulated supercell
932 structure and intensity to variations in the shapes of environmental buoyancy and
933 shear profiles. *Monthly Weather Review*, *129*(4), 664–687. https://doi.org/10.1175/
934 1520-0493(2001)129<0664:TSOSSS>2.0.CO;2

935 Mecikalski, J. R., & Bedka, K. M. (2006). Forecasting convective initiation by
936 monitoring the evolution of moving cumulus in daytime GOES imagery. *Monthly*
937 *Weather Review*, *134*(1), 49–78. https://doi.org/10.1175/MWR3062.1

938 Meng, Y., Sun, J., Zhang, Y., & Fu, S. (2021). A 10-year climatology of mesoscale
939 convective systems and their synoptic circulations in the southwest mountain area

of China. *Journal of Hydrometeorology*, *22*(1), 23–41. https://doi.org/10.1175/JHM-D-20-0167.1

Miao, Y., Guo, J., Liu, S., Liu, H., Li, Z., Zhang, W., & Zhai, P. (2017). Classification of summertime synoptic patterns in Beijing and their associations with boundary layer structure affecting aerosol pollution. *Atmospheric Chemistry and Physics*, *17*(4), 3097–3110. https://doi.org/10.5194/acp-17-3097-2017

Miller, D., & Fritsch, J. M. (1991). Mesoscale convective complexes in the western Pacific region. *Monthly Weather Review*, *119*(12), 2978–2992. https://doi.org/10.1175/1520-0493(1991)119<2978:MCCITW>2.0.CO;2

Morake, D. M., Blamey, R. C., & Reason, C. J. C. (2021). Long-lived mesoscale convective systems over eastern South Africa. *Journal of Climate*, *1*(aop), 1–66. https://doi.org/10.1175/JCLI-D-20-0851.1

Morel, C., & Senesi, S. (2002). A climatology of mesoscale convective systems over Europe using satellite infrared imagery. I: Methodology. *Quarterly Journal of the Royal Meteorological Society*, *128*(584), 1953–1971. https://doi.org/10.1256/003590002320603485

Nga, P. T. T., Ha, P. T., & Hang, V. T. (2021). Satellite-based regionalization of solar irradiation in Vietnam by k-Means clustering. *Journal of Applied Meteorology and Climatology*, *60*(3), 391–402. https://doi.org/10.1175/JAMC-D-20-0070.1

Ning, G., Yim, S. H. L., Yang, Y., Gu, Y., & Dong, G. (2020). Modulations of synoptic and climatic changes on ozone pollution and its health risks in mountain-basin areas. *Atmospheric Environment*, *240*, 117808. https://doi.org/10.1016/j.atmosenv.2020.117808

Panosetti, D., Böing, S., Schlemmer, L., & Schmidli, J. (2016). Idealized large-eddy and convection-resolving simulations of moist convection over mountainous terrain. *Journal of the Atmospheric Sciences*, *73*(10), 4021–4041. https://doi.org/10.1175/JAS-D-15-0341.1

Peters, J. M., & Schumacher, R. S. (2014). Objective categorization of heavy-rain-producing MCS synoptic types by rotated principal component analysis. *Monthly*

969 *Weather Review*, *142*(5), 1716–1737. https://doi.org/10.1175/MWR-D-13-00295.1

970 Punkka, A.-J., & Bister, M. (2015). Mesoscale convective systems and their synoptic-
971 scale environment in Finland. *Weather and Forecasting*, *30*(1), 182–196.
972 https://doi.org/10.1175/WAF-D-13-00146.1

973 Rasmussen, E. N., & Blanchard, D. O. (1998). A baseline climatology of sounding-
974 derived supercell and tornado forecast parameters. *Weather and Forecasting*, *13*(4),
975 1148–1164. https://doi.org/10.1175/1520-0434(1998)013<1148:ABCOSD>
976 2.0.CO;2

977 Rehbein, A., Ambrizzi, T., & Mechoso, C. R. (2018). Mesoscale convective systems
978 over the Amazon basin. Part I: climatological aspects. *International Journal of*
979 *Climatology*, *38*(1), 215–229. https://doi.org/10.1002/joc.5171

980 Reif, D. W., & Bluestein, H. B. (2017). A 20-year climatology of nocturnal convection
981 initiation over the central and southern Great Plains during the warm season.
982 *Monthly Weather Review*, *145*(5), 1615–1639. https://doi.org/10.1175/MWR-D-16-
983 0340.1

984 Roberts, R. D., & Rutledge, S. (2003). Nowcasting storm initiation and growth using
985 GOES-8 and WSR-88D data. *Weather and Forecasting*, *18*(4), 562–584.
986 https://doi.org/10.1175/1520-0434(2003)018<0562:NSIAGU>2.0.CO;2

987 Rodgers, D. M., Howard, K. W., & Johnston, E. C. (1983). Mesoscale convective
988 complexes over the United States during 1982. *Monthly Weather Review*, *111*(12),
989 2363–2369. https://doi.org/10.1175/1520-0493(1983)111<2363:
990 MCCOTU>2.0.CO;2

991 Rodgers, E. B., Chang, S. W., Stout, J., Steranka, J., & Shi, J.-J. (1991). Satellite
992 observations of variations in tropical cyclone convection caused by upper-
993 tropospheric troughs. *Journal of Applied Meteorology and Climatology*, *30*(8),
994 1163–1184. https://doi.org/10.1175/1520-0450(1991)030<1163:SOOVIT>
995 2.0.CO;2

996 Rousseeuw, P. J. (1987). Silhouettes: A graphical aid to the interpretation and validation
997 of cluster analysis. *Journal of Computational and Applied Mathematics*, *20*, 53–65.

https://doi.org/10.1016/0377-0427(87)90125-7

Shen, Y., Du, Y., & Chen, G. (2020). Ensemble sensitivity analysis of heavy rainfall associated with three MCSs coexisting over southern China. *Journal of Geophysical Research: Atmospheres*, *125*(2). https://doi.org/10.1029/2019JD031266

Shi, Y., Jiang, Z., Liu, Z., & Li, L. (2020). A Lagrangian analysis of water vapor sources and pathways for precipitation in East China in different stages of the east Asian summer monsoon. *Journal of Climate*, *33*(3), 977–992. https://doi.org/10.1175/JCLI-D-19-0089.1

Sieglaff, J. M., Cronce, L. M., Feltz, W. F., Bedka, K. M., Pavolonis, M. J., & Heidinger, A. K. (2011). Nowcasting convective storm initiation using satellite-based box-averaged cloud-top cooling and cloud-type trends. *Journal of Applied Meteorology and Climatology*, *50*(1), 110–126. https://doi.org/10.1175/2010JAMC2496.1

Solman, S. A., & Menéndez, C. G. (2003). Weather regimes in the South American sector and neighbouring oceans during winter. *Climate Dynamics*, *21*(1), 91–104. https://doi.org/10.1007/s00382-003-0320-x

Song, F., Feng, Z., Leung, L. R., Jr, R. A. H., Wang, J., Hardin, J., & Homeyer, C. R. (2019). Contrasting spring and summer large-scale environments associated with mesoscale convective systems over the U.S. Great Plains. *Journal of Climate*, *32*(20), 6749–6767. https://doi.org/10.1175/JCLI-D-18-0839.1

Stahl, K., Moore, R. D., & Mckendry, I. G. (2006). The role of synoptic-scale circulation in the linkage between large-scale ocean–atmosphere indices and winter surface climate in British Columbia, Canada. *International Journal of Climatology*, *26*(4), 541–560. https://doi.org/10.1002/joc.1268

Sugimoto, S., & Ueno, K. (2010). Formation of mesoscale convective systems over the eastern Tibetan Plateau affected by plateau-scale heating contrasts. *Journal of Geophysical Research: Atmospheres*, *115*. https://doi.org/10.1029/2009JD013609

Sun, J., & Zhang, F. (2012). Impacts of mountain–plains solenoid on diurnal variations of rainfalls along the mei-yu front over the East China plains. *Monthly Weather*

Review, *140*(2), 379–397. https://doi.org/10.1175/MWR-D-11-00041.1

Sun J., Wei J., Fu S., Zhang Y. & Wang H., 2018: The multi-scale physical model for persistent heavy rainfall events in the Yangtze-Huaihe River valley. *Chinese Journal of Atmospheric Sciences*, *42*(4), 741–754, http://doi.org/10.3878/j.issn.1006-9895.1803.17246. (in Chinese)

Tao, S. (1980). *Heavy Rainfalls in China*. Beijing: Science Press.

Ternynck, C., Alaya, M. A. B., Chebana, F., Dabo-Niang, S., & Ouarda, T. B. M. J. (2016). Streamflow hydrograph classification using functional data analysis. *Journal of Hydrometeorology*, *17*(1), 327–344. https://doi.org/10.1175/JHM-D-14-0200.1

Vandal, T., & Nemani, R. (2020). Temporal interpolation of geostationary satellite imagery with task specific optical flow. *Proceedings of 1st ACM SIGKDD Workshop on Deep Learning for Spatiotemporal Data, Applications, and Systems (DeepSpatial '20)*, 9 pp. http://mason.gmu.edu/~lzhao9/venues/DeepSpatial2020/papers/DeepSpatial_paper_6_camera_ready.pdf

Velasco, I., & Fritsch, J. M. (1987). Mesoscale convective complexes in the Americas. *Journal of Geophysical Research: Atmospheres*, *92*(D8), 9591–9613. https://doi.org/10.1029/JD092iD08p09591

Wang, H., Sun, J., Fu, S., & Zhang, Y. (2021). Typical circulation patterns and associated mechanisms for persistent heavy rainfall events over Yangtze-Huaihe River Valley during 1981–2020. *Advances in Atmospheric Sciences*, *38*(12), 2167–2182. https://doi.org/10.1007/s00376-021-1194-8

Williams, M., & Houze, R. A. (1987). Satellite-observed characteristics of winter monsoon cloud clusters. *Monthly Weather Review*, *115*(2), 505–519. https://doi.org/10.1175/1520-0493(1987)115<0505:SOCOWM>2.0.CO;2

Wilson, J. W., & Roberts, R. D. (2006). Summary of convective storm initiation and evolution during IHOP: observational and modeling perspective. *Monthly Weather Review*, *134*(1), 23–47. https://doi.org/10.1175/MWR3069.1

Yang, J., Zhang, Z., Wei, C., Lu, F., & Guo, Q. (2017). Introducing the new generation of Chinese geostationary weather satellites, Fengyun-4. *Bulletin of the American Meteorological Society*, *98*(8), 1637–1658. https://doi.org/10.1175/BAMS-D-16-0065.1

Yang, J., Zhao, K., Chen, X., Huang, A., Zheng, Y., & Sun, K. (2020). Subseasonal and diurnal variability in lightning and storm activity over the Yangtze River Delta, China, during mei-yu season. *Journal of Climate*, *33*(12), 5013–5033. https://doi.org/10.1175/JCLI-D-19-0453.1

Yang, R., Zhang, Y., Sun, J., & Li, J. (2020). The comparison of statistical features and synoptic circulations between the eastward-propagating and quasi-stationary MCSs during the warm season around the second-step terrain along the middle reaches of the Yangtze River. *Science China Earth Sciences*, *63*(8), 1209–1222. https://doi.org/10.1007/s11430-018-9385-3

Yang, X., Fei, J., Huang, X., Cheng, X., Carvalho, L. M. V., & He, H. (2015). Characteristics of mesoscale convective systems over China and its vicinity using geostationary satellite FY2. *Journal of Climate*, *28*(12), 4890–4907. https://doi.org/10.1175/JCLI-D-14-00491.1

Yang, X., & Sun, J. (2018). Organizational modes of severe wind-producing convective systems over North China. *Advances in Atmospheric Sciences*, *35*(5), 540–549. https://doi.org/10.1007/s00376-017-7114-2

Yang, Y., Wang, R., Chen, F., Liu, C., Bi, X., & Huang, M. (2021). Synoptic weather patterns modulate the frequency, type and vertical structure of summer precipitation over Eastern China: a perspective from GPM observations. *Atmospheric Research*, *249*, 105342. https://doi.org/10.1016/j.atmosres.2020.105342

Ying, M., Zhang, W., Yu, H., Lu, X., Feng, J., Fan, Y., et al. (2014). An overview of the China Meteorological Administration tropical cyclone database. *Journal of Atmospheric and Oceanic Technology*, *31*(2), 287–301. https://doi.org/10.1175/JTECH-D-12-00119.1

Yu, R., Zhou, T., Xiong, A., Zhu, Y., & Li, J. (2007). Diurnal variations of summer

precipitation over contiguous China. *Geophysical Research Letters*, *34*(1). https://doi.org/10.1029/2006GL028129

Zhang, A. Q., Chen, Y. L., Zhou, S. N., Cui, C. G., Wan, R., & Fu, Y. F. (2020). Diurnal variation of meiyu rainfall in the Yangtze Plain during atypical meiyu years. *Journal of Geophysical Research: Atmospheres*, *125*(1), e2019JD031742. https://doi.org/10.1029/2019JD031742

Zhang, X., Shen, W., Zhuge, X., Yang, S., Chen, Y., Wang, Y., Chen, T., & Zhang, S. (2021). Statistical characteristics of mesoscale convective systems initiated over the Tibetan Plateau in summer by Fengyun satellite and precipitation estimates. *Remote Sensing*, *13*(9). https://doi.org/10.3390/rs13091652

Zhang, X., Wang, X. L., & Corte-Real, J. (1997). On the relationships between daily circulation patterns and precipitation in Portugal. *Journal of Geophysical Research: Atmospheres*, *102*(D12), 13495–13507. https://doi.org/10.1029/97JD01012

Zhang, Y., & Sun, J. (2017). Comparison of the diurnal variations of precipitation east of the Tibetan Plateau among sub-periods of Meiyu season. *Meteorology and Atmospheric Physics*, *129*(5), 539–554. https://doi.org/10.1007/s00703-016-0484-7

Zhang, Y., Zhang, F., & Sun, J. (2014). Comparison of the diurnal variations of warm-season precipitation for East Asia vs. North America downstream of the Tibetan Plateau vs. the Rocky Mountains. *Atmospheric Chemistry and Physics*, *14*(19), 10741–10759. https://doi.org/10.5194/acp-14-10741-2014

Zhang, Y., Zhang, F., Davis, C. A., & Sun, J. (2018). Diurnal evolution and structure of long-lived mesoscale convective vortices along the mei-yu front over the East China plains. *Journal of the Atmospheric Sciences*, *75*(3), 1005–1025. https://doi.org/10.1175/JAS-D-17-0197.1

Zheng, L., Sun, J., Zhang, X., & Liu, C. (2013). Organizational modes of mesoscale convective systems over Central East China. *Weather and Forecasting*, *28*(5), 1081–1098. https://doi.org/10.1175/WAF-D-12-00088.1

Zheng, Y., Chen, J., & Zhu, P. (2008). Climatological distribution and diurnal variation

of mesoscale convective systems over China and its vicinity during summer. *Chinese Science Bulletin*, *53*(10), 1574–1586. https://doi.org/10.1007/s11434-008-0116-9

Zhu, L., Liu, J., Zhu, A., Sheng, M., & Duan, Z. (2018). Spatial distribution of diurnal rainfall variation in summer over China. *Journal of Hydrometeorology*, *19*(4), 667–678. https://doi.org/10.1175/JHM-D-17-0176.1

Zipser, E. J. (1977). Mesoscale and convective–scale downdrafts as distinct components of squall-line structure. *Monthly Weather Review*, *105*(12), 1568–1589. https://doi.org/10.1175/1520-0493(1977)105<1568:MACDAD>2.0.CO;2